Digital Discovery

rsc.li/digitaldiscovery

Quantum Simulation

ROYAL SOCIETY
OF **CHEMISTRY**
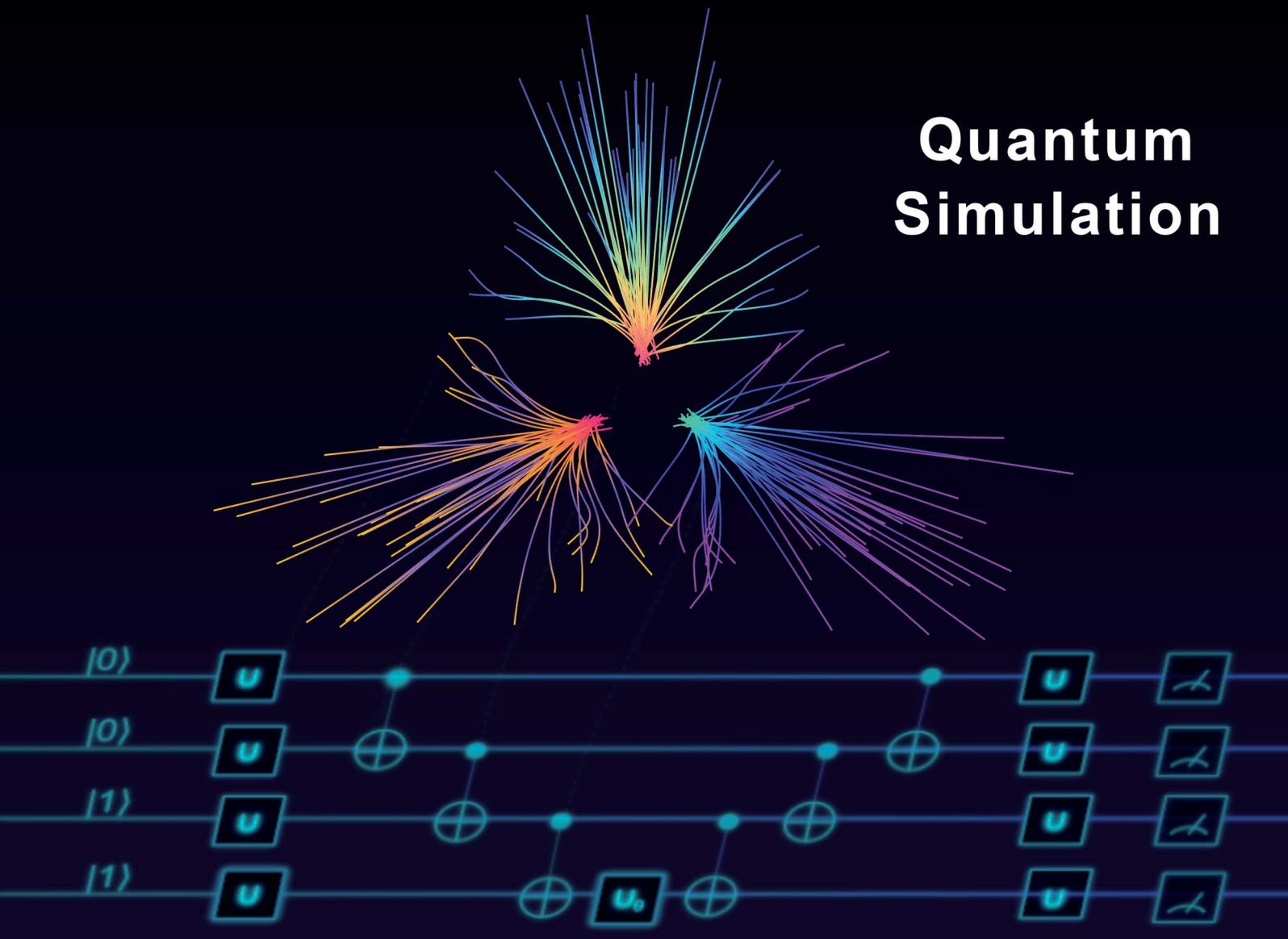
PAPER
Diandong Tang, Xiaoxia Cai, Xiao Yuan *et al.*
Efficient quantum simulation of non-adiabatic molecular
dynamics with precise electronic structure

Check for updates

Efficient quantum simulation of non-adiabatic molecular dynamics with precise electronic structure

Tianyi Li, [ID] ab Yumeng Zeng,a Qiming Ding, [ID] a Zixuan Huo,a Xiaosi Xu,c Jiajun Ren,d Diandong Tang, [ID] *e Xiaoxia Cai*f and Xiao Yuan*a

In the study of non-adiabatic chemical processes such as photocatalysis and photosynthesis, non-adiabatic molecular dynamics (NAMD) is an indispensable theoretical tool, which requires precise potential energy surfaces (PESs) of ground and excited states. Quantum computing offers promising potential for calculating PESs that are intractable for classical computers. However, its realistic application poses significant challenges to the development of quantum algorithms that are sufficiently general to enable efficient and precise PES calculations across chemical systems with diverse properties and to seamlessly adapt existing NAMD theories to quantum computing. In this work, we introduce a quantum-adapted extension to the Landau–Zener-Surface-Hopping (LZSH) NAMD. This extension incorporates curvature-driven hopping corrections that protect the population evolution while maintaining the efficiency gained from avoiding the computation of non-adiabatic couplings (NACs) and preserving the trajectory independence that enables parallelization. Furthermore, to ensure the high-precision PESs required for surface hopping dynamics, we develop a sub-microhartree-accurate PES calculation protocol. This protocol supports active space selection, enables parallel acceleration either on quantum or classical clusters, and demonstrates adaptability to diverse chemical systems—including the charged H_3^+ ion and the C_2H_4 molecule, a prototypical multi-reference benchmark. This work paves the way for practical application of quantum computing in NAMD, showcasing the potential of parallel simulation on quantum-classical heterogeneous clusters for *ab initio* computational chemistry.

Introduction

Ab initio molecular dynamics (AIMD) simulations are indispensable for elucidating mechanisms underlying chemical and biological processes, providing atomistic insights into phenomena ranging from charge carrier dynamics in materials,[1] excited-state dynamics of transition metal complexes,[2] and proton transfer in solvation processes[3] to photochemical reactions.[4,5] A foundational early approach of AIMD is the Born–Oppenheimer molecular dynamics framework, which leverages the Born–Oppenheimer approximation to decouple electronic and nuclear degrees of freedom. This approach has been proven

valuable for simulating equilibrium properties and slow dynamic processes in systems where the Born–Oppenheimer approximation holds.[6–9]

However, the Born–Oppenheimer approximation breaks down when the energy gap between electronic states becomes close, leading to strong non-adiabatic effects, which is crucial for understanding a broad spectrum of chemical phenomena. This occurs in scenarios involving conical intersections, avoided crossings, or ultra-fast electronic transitions, such as in photochemistry,[10–12] charge transfer,[13–15] or vibronic relaxation processes.[16–23] Under these conditions, Born–Oppenheimer molecular dynamics fails to capture the traveling of nuclear wavepackets across multiple potential energy surfaces (PESs) and is not able to describe excited-state dynamics and simulate photophysics and photochemistry reactions.

To fully simulate those processes, non-adiabatic molecular dynamics (NAMD) is necessary. Full quantum dynamics treats both electronic and nuclear degrees of freedom quantum mechanically, with the multi-configurational time-dependent Hartree[24] method being a prominent example; however, its computational cost escalates rapidly with system size. In contrast, mixed quantum-classical dynamics approximates nuclear motion classically while retaining quantum-mechanical

aCenter on Frontiers of Computing Studies, School of Computer Science, Peking University, Beijing 100871, China. E-mail: xiaoyuan@pku.edu.cn

bÉcole Normale Supérieure Paris-Saclay, Université Paris-Saclay, 91190 Gif-sur-Yvette, France

cGraduate School of China Academy of Engineering Physics, Beijing 100193, China

dKey Laboratory of Theoretical and Computational Photochemistry, Ministry of Education, College of Chemistry, Beijing Normal University, Beijing 100875, China

eDepartment of Chemistry, University of Washington, Seattle, WA 98195-1700, USA. E-mail: tangdd@uw.edu

fInstitute of High Energy Physics, Chinese Academy of Sciences, Beijing 100049, China. E-mail: xxcai@ihep.ac.cn

treatment of electrons, enabling efficient simulations of larger systems over relevant timescales. Several schemes fall under this category, including mean-field approaches, *ab initio* multiple spawning, and trajectory surface hopping.[25–28] Among surface hopping methods, the widely adopted fewest switches surface hopping (FSSH)[29] propagates nuclear trajectories classically on a single active PES while allowing stochastic hops between states based on transition probabilities. These probabilities are computed equally from three key quantities: non-adiabatic coupling (NAC), which represents the interaction between electronic states induced by nuclear motion; the nuclear time step, which scales the probability to ensure proper integration over the trajectory; and electronic coefficients, which encode the quantum amplitudes and coherences among states—though the update of these electronic coefficients itself relies on NAC to capture non-adiabatic effects during propagation. In addition to NAC, energy gaps between PESs and their derivatives offer more accessible electronic properties for driving state transitions, leading to efficient variants such as Landau–Zener-Surface-Hopping (LZSH),[30] Zhu–Nakamura surface hopping (ZNSH),[31–33] and curvature-driven surface hopping (κSH).[34–36] These protocols construct hopping events without explicit computation of NAC, making them well-suited for interfacing with electronic structure methods that may not readily provide such quantities.[37]

Despite these advances, solving the multi-state electronic structure remains a major challenge for NAMD on classical computers. Accurate treatment of conical intersections and strongly correlated systems often requires full configuration interaction (FCI), which scales exponentially with the number of orbitals and electrons, necessitating an exponential number of Slater determinants,[38] which is intractable for classical computers. While density functional theory (DFT) provides a computationally efficient alternative with $O(N^3)$ or $O(N^4)$ scaling, it faces challenges in accurately describing multi-configurational wavefunctions and excitation energies in non-adiabatic regimes.[39,40] These challenges motivate the exploration of quantum algorithms, which inherently exploit superposition and entanglement to efficiently solve the electronic Schrödinger equation for correlated systems, promising exponential speedups for NAMD in regimes inaccessible to classical-computing methods.[41–43]

Quantum algorithms for chemistry simulation are exemplified by the quantum phase estimation (QPE) method in the fault-tolerant quantum computing (FTQC) regime, which can theoretically achieve accuracy comparable to FCI, provided a suitable initial state is prepared (*e.g.*, *via* adiabatic state preparation).[44,45] Nevertheless, current quantum devices fall short in supporting QPE circuits of practical width, depth, qubit fidelity, and gate fidelity, compounded by the immaturity of quantum error correction. Near-term quantum algorithms, represented by Variational Quantum Eigensolver (VQE), offer a compromise by adopting a heuristic time complexity and tolerating moderate noise levels.[46,47] Grounded in the variational principle, VQE optimizes parametrized quantum circuits to approximate molecular energy spectra and corresponding electronic states. For larger-scale systems, the second-

quantization on which the VQE framework is based enables the selection of chemically significant molecular orbitals (MOs), forming an active space that captures essential chemical properties within constrained circuit sizes.[45,48] This complete active space (CAS) method is particularly vital for extending quantum-computing simulations to realistic molecular systems without exceeding resources of noisy intermediate-scale quantum (NISQ).[49]

Advancements in NISQ algorithms have significantly enhanced the computation of molecular excited states. Among these, the variational quantum deflation (VQD) method extends the VQE by incorporating overlap penalties to enforce approximate orthogonality with previously computed states, enabling sequential search of higher-energy eigenstates.[50,51] However, its iterative framework escalates computational demands, limits parallelization, and propagates errors in noisy settings. In contrast, subspace-based approaches enhance efficiency by restricting calculations to predefined excitation sectors. For instance, the subspace-search VQE (SSVQE) simultaneously optimizes a set of orthogonal initial states, reducing optimization iterations compared to serial search.[52] Complementing subspace concepts with a sampling strategy, sample-based quantum diagonalization (SQD) constructs and diagonalizes effective Hamiltonian matrices *via* quantum sampling, claimed to support large qubit systems and mitigate noise effects, yet it relies heavily on ample sampling for achieving high precision.[53,54] Building on similar foundations, Quantum Subspace Expansion (QSE) employs explicit projections onto Fermionic subspaces, yielding physically guaranteed variational upper bounds for excited-state energies.[55–58] Another prominent approach, the quantum equation-of-motion (QEOM), leverages subspace concepts while incorporating equation-of-motion (EOM) formalisms in classical-computing quantum chemistry, could ensure size-intensity and inherently introduce the contribution of de-excitation.[59–61] However, for QSE and QEOM, the choice and number of operators used in subspace construction determine the algorithm's ability to capture physical properties[62] and efficiency and robustness. The exquisite design of subspaces tailored to specific systems remains an on-going topic. Furthermore, to meet the NISQ constraints, optimization strategies at the implementation level leave a valuable area for exploration.

In this work, we introduce a practical quantum-computing NAMD framework, seamlessly integrated with our sub-microhartree-accuracy calculations of PESs across diverse chemical systems, including H_3^+ and C_2H_4, and compatible with parallel acceleration on both real quantum computers and quantum algorithm simulators on classical computers. While recent explorations[62,63] have advanced quantum-computing electronic structure solvers by comparing methods such as QEOM, QSE, and de-excited QSE, or employing VQD for sequential orthogonal excited-state searches, our approach pursues a distinct goal of achieving sub-microhartree precision through a hybrid subspace-based quantum-computing electronic structure solver that adapts operator selections to different chemicals, enhancing accuracy *via* problem-adapted subspace operator selection and integration of SSVQE for
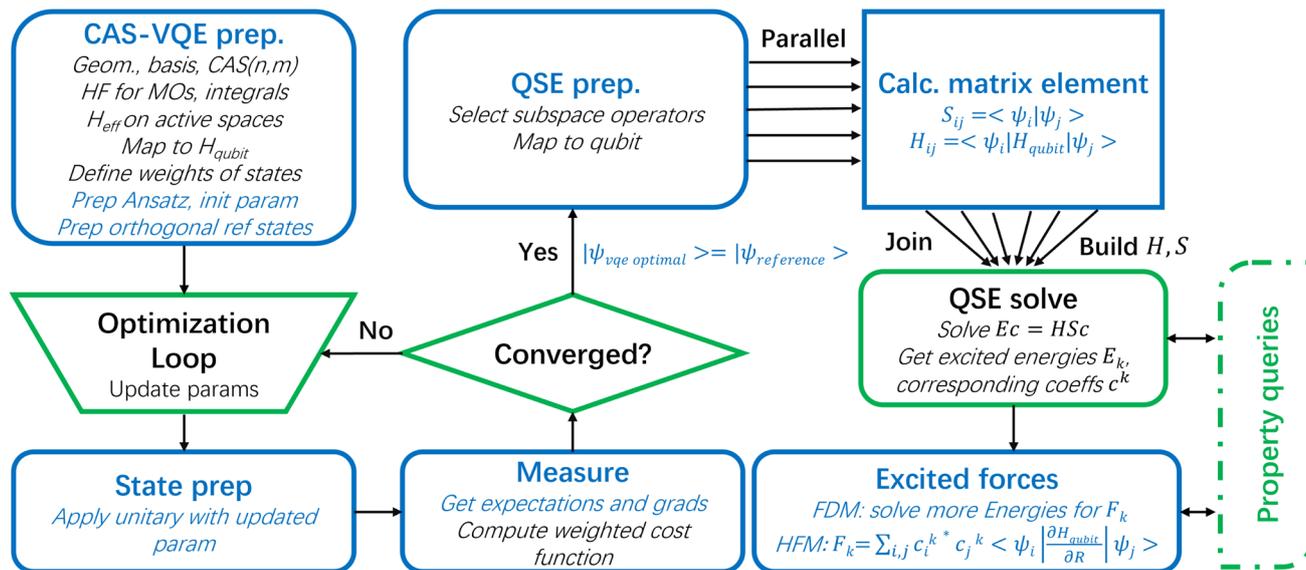
Fig. 1 Work flow of on-the-fly quantum solver for electronic-structure observables, with parallelization of QSE.

parallel optimization of multiple reference states prior to QSE application. We also rigorously assess the numerical stability of quantum-computed PESs and incorporate an efficient curvature-driven correction scheme for state transitions tailored to quantum-computing electronic structure solvers. In the NAMD evolution, whereas prior studies focused on FSSH requiring NAC computations, we focus on adapting LZSH for quantum algorithms, introducing an improved LZSH scheme that stabilizes dynamics more efficiently. These innovations, combined with a two-level parallelization framework and task-specific algorithmic extensions, yield substantial speedups without compromising PES precision, collectively elevating the robustness, efficiency, and practical viability of quantum-enhanced LZSH-NAMD simulations for broader chemical research (Fig. 1).

Methods

Capturing molecular properties on a quantum computer

Solving the electronic structure in active spaces. To simulate the molecular electronic structure on a quantum computer with flexibility, we employ the second-quantized representation of the molecular Hamiltonian within a selected complete active space (CAS).[64] In quantum chemistry, CAS classifies molecular orbitals into core (always doubly occupied), active (partially occupied), and virtual (always unoccupied) sets, generating a wavefunction as a configuration interaction expansion within the active orbitals, which resolves the electron correlation problem in strongly correlated systems such as bond dissociation or transition metal complexes.

The electronic molecular Hamiltonian in second quantization is expressed as[65]

$$\hat{H} = \sum_{pq} h_{pq} \hat{a}_p^\dagger \hat{a}_q + \frac{1}{2} \sum_{pqrs} g_{pqrs} \hat{a}_p^\dagger \hat{a}_q^\dagger \hat{a}_r \hat{a}_s, \qquad (1)$$

where $\hat{a}_p^\dagger$ and $\hat{a}_p$ are the fermionic creation and annihilation operators for orbital p, h_{pq} are the one-electron integrals, and g_{pqrs} are the two-electron integrals. These integrals are obtained using classical-computing quantum chemistry software, typically through Hartree–Fock calculations. The indices p, q, r, and s run over the MOs.

In the CAS framework,[66] we partition the orbitals into core (inactive), active, and virtual (inactive) sets. The core orbitals are doubly occupied, and their contributions are incorporated into an effective one-electron potential. The active space consists of m orbitals and n electrons, where strong correlations are expected, such as in bond-breaking regions or excited states. Selecting the active orbitals is crucial for accuracy and efficiency. General strategies include identifying orbitals based on chemical intuition, such as valence orbitals involved in bonding or antibonding interactions, or using orbital energies and occupancies from preliminary calculations. For smaller active spaces (e.g., CAS(2,2) or CAS(4,4)), manual selection is common, visualizing molecular orbitals from Hartree–Fock calculations to choose frontier orbitals such as the highest occupied molecular orbital, the lowest unoccupied molecular orbital, or those directly participating in the chemical process of interest, ensuring that the space captures the dominant static correlation with minimal computational cost. For larger active spaces (e.g., CAS(10,10) or beyond), automated strategies are preferred to handle complexity, such as the ranked-orbital approach,[67] entropy-based selection from uncorrelated natural orbitals combined with the density matrix renormalization group,[68] or machine learning selection,[69] which systematically expand the space while maintaining convergence. In this work, we use a selection strategy based on orbital energies and occupancies from preliminary calculations, where the active space comprises contiguous frontier orbitals around the Fermi level to efficiently capture dominant static correlations.

The Hamiltonian is then restricted to excitations within this active space, yielding

$$\hat{H}_{AS} = \sum_{pq \in AS} h_{pq}^{eff} \hat{a}_p^\dagger \hat{a}_q + \frac{1}{2} \sum_{pqrs \in AS} g_{pqrs} \hat{a}_p^\dagger \hat{a}_q^\dagger \hat{a}_r \hat{a}_s, \tag{2}$$

where h_{pq}^{eff} includes corrections from the inactive orbitals.

Since quantum computers operate on qubits rather than fermions, the fermionic Hamiltonian must be mapped to a qubit Hamiltonian to enable simulation via quantum circuits. To achieve this, we apply the Jordan–Wigner (JW) transformation.[70] The JW mapping encodes fermionic operators into an O(1) number of Pauli strings as

$$\hat{a}_p^\dagger = \frac{1}{2}(X_p - iY_p) \prod_{j=0}^{p-1} Z_j, \quad \hat{a}_p = \frac{1}{2}(X_p + iY_p) \prod_{j=0}^{p-1} Z_j, \tag{3}$$

where X_p, Y_p, and Z_p are Pauli operators acting on qubit p, and the product of Z operators enforces Fermionic anti-commutation relations. This transformation requires $2m$ qubits for a spin–orbital basis (or m qubits with spin-symmetry adaptations). Substituting eqn (3) into (2) results in a qubit Hamiltonian

$$\hat{H}_{qubit} = \sum_k c_k \hat{P}_k, \tag{4}$$

where $\hat{P}_k$ are Pauli strings mapped from effective one-electron integral terms and two-electron integral terms and c_k are coefficients obtained by summing the coefficients of the same Pauli strings.

Variational quantum algorithms for the reference state. The VQE is employed to approximate the ground state of the qubit Hamiltonian. VQE leverages the variational principle, minimizing the expectation value $\langle \hat{H}_{qubit} \rangle$ over a parametrized quantum state $|\psi(\boldsymbol{\theta})\rangle_{QC}$, prepared on a quantum circuit.[71] The ansatz state is generated by applying a unitary operator $\hat{U}(\boldsymbol{\theta})$ to an initial reference state $|\Phi_0\rangle$, typically the Hartree–Fock state:[71]

$$|\psi(\boldsymbol{\theta})\rangle_{QC} = \hat{U}(\boldsymbol{\theta})|\Phi_0\rangle. \tag{5}$$

Common ansatzes include the unitary coupled-cluster (UCC) form, such as UCCSD, which approximates the exponential cluster operator:[71]

$$\hat{U}(\boldsymbol{\theta}) = \exp\left(\sum_i \theta_i \hat{\tau}_i - \theta_i^* \hat{\tau}_i^\dagger\right), \tag{6}$$

where $\hat{\tau}_i$ are excitation operators mapped to qubits. The energy expectation value is

$$E(\boldsymbol{\theta}) = \langle \psi(\boldsymbol{\theta})|\hat{H}_{qubit}|\psi(\boldsymbol{\theta})\rangle_{QC} = \sum_k c_k \langle \hat{P}_k \rangle, \tag{7}$$

and is evaluated by measuring the Pauli strings on the quantum device. Classical-computing optimization algorithms, such as gradient descent or BFGS, minimize $E(\boldsymbol{\theta})$ to find the optimal parameters $\boldsymbol{\theta}^*$.[72] Building upon the CAS and the VQE framework, the derived method provides a powerful hybrid approach for NISQ simulation. Here, VQE is applied to variationally solve the eigenvalue problem within the active space, serving as

a quantum analogy to classical-computing CASCI.[73] Classical-computing CASCI expresses the wave function as a full linear combination of Slater determinants in the active space and solves the eigenstates via direct diagonalization. However, on the classical computer, the active space dimension grows factorially with the number of active orbitals and electrons, making classical-computing CASCI intractable for large spaces. The CAS-VQE method makes this tractable by exploiting quantum computers' ability to encode spin orbitals,[74] where the VQE ansatz spans the Hilbert space of active orbitals and gives compact parametrization of correlations.[75] Optimization of the CAS-VQE follows standard VQE but employs the active space-restricted Hamiltonian, simulating only relevant electronic degrees of freedom. This enables accurate ground-state energies in static-correlation regimes while ensuring computational tractability.

Beyond the canonical single-reference VQE in selected active spaces, multi-reference features can be incorporated to enhance the ground-state search in systems exhibiting strong static correlation. One such extension is the SSVQE, which expands the variational search into a larger subspace spanned by multiple orthogonal reference states[52] in selected active spaces.

In SSVQE, a set of k mutually orthogonal initial reference states $\{|\phi_j\rangle\}_{j=1}^k$ is selected, often including the Hartree–Fock state and additional configurations to introduce multi-reference features. The same parametrized unitary operator $\hat{U}(\boldsymbol{\theta})$ is applied to each reference, producing trial states $|\psi_j(\boldsymbol{\theta})\rangle = \hat{U}(\boldsymbol{\theta})|\phi_j\rangle$. The variational cost function is defined as a weighted sum of the energy expectation values:

$$E(\boldsymbol{\theta}) = \sum_{j=1}^k w_j \langle \psi_j(\boldsymbol{\theta})|\hat{H}|\psi_j(\boldsymbol{\theta})\rangle, \tag{8}$$

where the weights w_j could be chosen to be positive and decreasing ($w_1 > w_2 > \ldots > w_k > 0$) to encourage the mapping of the trial states onto the lowest-energy eigenstates of the Hamiltonian. Classical-computing optimization minimizes $E(\boldsymbol{\theta})$ to yield optimal parameters $\boldsymbol{\theta}^*$, effectively projecting the initial subspace onto the low-lying eigensubspace. The lowest-energy state among the optimized set, typically $|\psi_0(\boldsymbol{\theta}^*)\rangle$, serves as the variational ground state.

Quantum subspace expansion toolbox for excited states. To access excited states in quantum computing simulations, the QSE method projects the Hamiltonian into a subspace spanned by variationally prepared states and their excitations, followed by classical-computing diagonalization of the subspace Hamiltonian to obtain excited states.[55] This approach provides a physically ensured way of calculating excited states with a given reference state and avoids the limitations of methods relying on parameter optimization.

In the Tamm-Dancoff Approximation for QSE (TDA-QSE),[76] the subspace is constructed by applying low-rank excitation operators $\hat{E}_\mu$ to a reference state $|\psi_k\rangle_{QC}$, generating basis vectors; the excitations only include single excitations $\hat{a}_p^\dagger \hat{a}_q$ and double excitations $\hat{a}_p^\dagger \hat{a}_q^\dagger \hat{a}_r \hat{a}_s$:

$$|\phi_\mu\rangle = \hat{E}_\mu |\psi_k\rangle_{QC}. \tag{9}$$

Note that the reference state $|\psi_k\rangle_{QC}$ is prepared on a quantum circuit by applying the optimal gate parameters (which are given by VQE) onto the ansatz circuit (*i.e.* UCCSD).The projected Hamiltonian and overlap matrices are defined as

$$H_{\mu\nu} = \langle\phi_\mu|\hat{H}_{qubit}|\phi_\nu\rangle, \quad S_{\mu\nu} = \langle\phi_\mu|\phi_\nu\rangle, \quad (10)$$

$$\mathbf{Hc} = E\mathbf{Sc}. \quad (11)$$

The Fermion operators $\hat{E}_\mu$ and $\hat{E}_\nu$ could be transformed and decomposed into the $\mathcal{O}(1)$ number of Pauli operators by the Jordan–Wigner transformation just like how $\hat{H}_{AS}$ transformed into $\hat{H}_{qubit}$ in eqn (3). Excited-state energies and eigenvectors are obtained by solving the generalized eigenvalue problem:

The number of matrix elements scales as $\mathcal{O}(m^8)$, where m is the number of selected orbitals. This results in an overall operator complexity of $\mathcal{O}(m^4)$.

Beyond TDA-QSE, the general QSE framework supports a versatile set of fermionic operators in second quantization, enabling flexible subspace construction for systems with specific electron structures, such as those near conical intersections or avoided crossings. Each operator has an inverse (its Hermitian adjoint, *e.g.*, de-excitations for excitations), which can enhance the description of physical properties.[62] Below, we list extensible operator classes, their second quantization forms, and their computational complexities, assuming a spin-orbital basis with m active spatial orbitals. Summations (*e.g.*, p > q) ensure proper antisymmetrization, and spin-adapted forms[77] are used where applicable to target singlet states ($S^2 = 0$).

• Higher-order excitations: these extend single and double excitations to triples, quadruples, and beyond, capturing higher-order electron correlations critical for multi-reference systems. For a triple excitation (from occupied orbitals i, j, and k to virtual orbitals a, b, and c):

$$\hat{E}^{abc}_{ijk} = a\hat{a}^\dagger_a\hat{a}^\dagger_b\hat{a}^\dagger_c\hat{a}_k\hat{a}_j\hat{a}_i. \quad (12)$$

The inverse is $\hat{E}^{ijk}_{abc} = a\hat{a}^\dagger_i\hat{a}^\dagger_j\hat{a}^\dagger_k\hat{a}_c\hat{a}_b\hat{a}_a$. The number of triple excitation operators scales as $\mathcal{O}(m^6)$, quadruples as $\mathcal{O}(m^8)$, and general k-th order excitations as $\mathcal{O}(m^{2k})$, with de-excitations sharing the same complexity. Spin-adapted forms, constructed analogously to single and double excitations, commute with $\hat{S}^2$, reducing the constant factor in the subspace dimension.

• Spin-flip operators: these alter spin multiplicity by flipping electron spins while conserving orbital occupancy, useful for describing open-shell configurations. A single spin-flip (*e.g.*, α to β in orbitals p and q):

$$\widehat{SF}_{p\beta,q\alpha} = \hat{a}^\dagger_{p\beta}\hat{a}_{q\alpha}. \quad (13)$$

The inverse is $\hat{a}^\dagger_{q\alpha}\hat{a}_{p\beta}$. Double spin-flips are naturally spin-adapted and follow similarly (*e.g.*, $\hat{a}^\dagger_{p\beta}\hat{a}^\dagger_{q\beta}\hat{a}_{s\alpha}\hat{a}_{r\alpha}$). Single spin-flips scale as $\mathcal{O}(m^2)$ and double spin-flips as $\mathcal{O}(m^4)$. These operators are not naturally restricted to singlet states, as they couple different spin sectors, increasing the subspace dimension unless filtered by $\hat{S}^2$ commutation.

• Spin-mixing operators: these couple different spin sectors without flipping spins, enabling transitions between states of differing spin multiplicities while preserving total spin projection. A representative operator:

$$\hat{M}_{pqrs} = \hat{a}^\dagger_{p\alpha}\hat{a}^\dagger_{q\beta}\hat{a}_{s\beta}\hat{a}_{r\alpha}. \quad (14)$$

The inverse is $\hat{a}^\dagger_{r\alpha}\hat{a}^\dagger_{s\beta}\hat{a}_{q\beta}\hat{a}_{p\alpha}$. These operators scale as $\mathcal{O}(m^4)$ and, like spin-flip operators, are not inherently restricted to singlets, requiring $\hat{S}^2$ filtering to target singlet states.

• Orbital rotations: these unitary transformations mix orbitals within the active space, optimizing orbital bases for response properties or strong correlation. The generator is anti-Hermitian:

$$\hat{\kappa} = \sum_{p>q}\kappa_{pq}\left(\hat{a}^\dagger_{p\alpha}\hat{a}_{q\alpha} - \hat{a}^\dagger_{q\alpha}\hat{a}_{p\alpha} + \hat{a}^\dagger_{p\beta}\hat{a}_{q\beta} - \hat{a}^\dagger_{q\beta}\hat{a}_{p\beta}\right). \quad (15)$$

The inverse is $-\hat{\kappa}$, as $(\hat{\kappa})^\dagger = -\hat{\kappa}$. Orbital rotations scale as $\mathcal{O}(m^2)$ and are naturally spin-adapted, commuting with $\hat{S}^2$, making them efficient for singlet subspaces.

• Non-diagonal couplings: these couple configurations across the orbital space without strict occupancy constraints, enhancing subspace flexibility. A general non-diagonal double coupling:

$$\hat{C}_{pqrs} = \hat{a}^\dagger_p\hat{a}^\dagger_q\hat{a}_s\hat{a}_r. \quad (16)$$

The inverse is $\hat{a}^\dagger_r\hat{a}^\dagger_s\hat{a}_q\hat{a}_p$. These operators scale as $\mathcal{O}(m^4)$, and the inverse form would be in the form of $\hat{a}^\dagger_r\hat{a}^\dagger_s\hat{a}_q\hat{a}_p$. Spin adaptation could be achieved by symmetrically (or antisymmetrically) combining α–β pairs, yielding operators that commute with $\hat{S}^2$ and reduce the effective dimensionality of the excitation subspace.

• Electron–electron interaction operators: these directly incorporate two-body interaction terms from the molecular Hamiltonian, capturing dynamic and static electron correlations. These are derived from the Hamiltonian's two-electron integrals V_{pqrs}. Including these operators enhances the subspace's ability to describe correlation effects, but requires careful selection of significant integrals (*e.g.*, $|V_{pqrs}| > \varepsilon$) to manage computational cost. A representative operator is

$$\hat{V}_{pqrs} = g_{pqsr}\hat{a}^\dagger_p\hat{a}^\dagger_q\hat{a}_s\hat{a}_r. \quad (17)$$

The inverse is $\hat{a}^\dagger_r\hat{a}^\dagger_s\hat{a}_q\hat{a}_p$. The number of such operators scales as $\mathcal{O}(m^4)$, matching double excitations. Spin-adapted forms are constructed similarly by ensuring commutation with $\hat{S}^2$.

Implementation-level adaptations and optimizations could ameliorate the constant-factor overhead. When the number of selected expansion operators is large, the S matrix may become ill-conditioned.[78] We could adopt regularization methods to maintain numerical stability at the implementation level.[79]

Beyond its role in accessing excited states, QSE also serves as a powerful quantum error mitigation technique by projecting noisy or non-optimal reference states into a carefully constructed subspace that isolates and corrects errors inherent to near-term quantum hardware.[80–82] In this context, QSE leverages excitation operators to expand the reference state, enabling the identification and suppression of noise-induced artifacts through the diagonalization of the projected Hamiltonian and

overlap matrices, effectively restoring physical fidelity without requiring full error correction protocols. This application of QSE for error mitigation represents a distinct research branch, complementary to its excited-state computations, with ongoing developments focusing on adaptive operator selection and regularization to enhance robustness against quantum errors.

Obtaining nuclear force. To simulate the time evolution of the molecular system in the context of surface hopping dynamics, quality nuclear forces are essential. These forces are derived from the gradients of the PESs corresponding to different electronic states.[83,84]

In our approach, the reference state $|\Psi_0\rangle$ is obtained using VQE or SSVQE. Excited states could be constructed using the result of QSE, where the excited state wavefunctions $|\Psi_k\rangle$ (for $k \geq 1$) could be written as linear combinations of the reference state and applications of excitation operators E_i:[57]

$$|\Psi_k\rangle = c_{k0}|\Psi_0\rangle + \sum_{i=1}^{M} c_{ki}E_i|\Psi_0\rangle, \qquad (18)$$

where $\boldsymbol{c}_k = (c_{k0}, c_{k1}, \ldots, c_{kM})^T$ is the k-th eigenvector from the QSE diagonalization and E_i are excitation operators. The coefficients $\boldsymbol{c}_k$ are obtained by solving the generalized eigenvalue problem in the QSE subspace. Note that this does not mean to explicitly prepare an excited-state wave function on a quantum computer, but through such representation, we could finally construct observables and estimate corresponding expectations as in 25.

Nuclear forces are the negative gradients of the electronic energy with respect to nuclear coordinates $\mathbf{R}$:

$$\mathbf{F}_k(\mathbf{R}) = -\nabla_{\mathbf{R}} E_k(\mathbf{R}), \qquad (19)$$

where $E_k(\mathbf{R}) = \langle \Psi_k | \hat{H}(\mathbf{R}) | \Psi_k \rangle$ is the energy of the k-th state and $\hat{H}(\mathbf{R})$ is the molecular Hamiltonian.

Two primary methods exist for computing these gradients: the finite difference method (FDM) and Hellmann–Feynman method (HFM).

The FDM provides a numerical gradient. It could approximate the gradient *via* central differences[85]

$$\frac{\partial E_k}{\partial R_\alpha} \approx \frac{E_k(\mathbf{R} + \varepsilon\boldsymbol{e}_\alpha) - E_k(\mathbf{R} - \varepsilon\boldsymbol{e}_\alpha)}{2\varepsilon}, \qquad (20)$$

where ε is the displacement step size and $\boldsymbol{e}_\alpha$ is the unit vector along coordinate α.

The HFM provides analytical gradients. The Hellmann–Feynman theorem states that for an exact or variationally optimized wavefunction $|\Psi\rangle$ of a Hamiltonian $\hat{H}(\lambda)$ depending on a parameter λ, the derivative of the energy $E(\lambda) = \langle \Psi | \hat{H} | \Psi \rangle$ (assuming normalization $\langle \Psi | \Psi \rangle = 1$) with respect to λ is given by[86,87]

$$\frac{dE}{d\lambda} = \left\langle \Psi \left| \frac{\partial \hat{H}}{\partial \lambda} \right| \Psi \right\rangle. \qquad (21)$$

This result follows from differentiating the energy expression:

$$\frac{dE}{d\lambda} = \left\langle \frac{\partial \Psi}{\partial \lambda} \middle| \hat{H} \middle| \Psi \right\rangle + \left\langle \Psi \left| \frac{\partial \hat{H}}{\partial \lambda} \right| \Psi \right\rangle + \left\langle \Psi \middle| \hat{H} \middle| \frac{\partial \Psi}{\partial \lambda} \right\rangle. \qquad (22)$$

If $|\Psi\rangle$ is a normalized eigenstate of $\hat{H}$, the sum $\left\langle \frac{\partial \Psi}{\partial \lambda} \middle| \hat{H} \middle| \Psi \right\rangle + \left\langle \Psi \middle| \hat{H} \middle| \frac{\partial \Psi}{\partial \lambda} \right\rangle$ vanishes, as required by the eigenvalue equation $(\hat{H} - E)|\Psi\rangle = 0$ and the normalization condition $\langle \Psi | \Psi \rangle = 1$. Furthermore, upon adopting a gauge where the global phase of $|\Psi(\lambda)\rangle$ is chosen such that $\left\langle \Psi \middle| \frac{\partial \Psi}{\partial \lambda} \right\rangle = 0$, each term vanishes individually. For a variationally prepared wavefunction, if it is optimal with respect to its parameters, the response term will be zero by the variational principle, making the theorem applicable to states given by VQE or QSE.[87]

In implementation, we would use the finite basis set to construct the wave function. When using atom-centered basis sets (*e.g.*, Gaussian orbitals), the basis functions will depend implicitly on nuclear positions, and since λ corresponds to nuclear coordinates R_α, the force will be $-\langle \Psi | \partial \hat{H} / \partial R_\alpha | \Psi \rangle$. This would introduce additional contributions known as Pulay terms or Pulay forces. These arise because the derivative must account for the basis set's coordinate dependence:[88]

$$\frac{\partial \hat{H}}{\partial R_\alpha} = \frac{\partial \hat{H}}{\partial R_\alpha}\bigg|_\chi + \sum_{\mu\nu} \frac{\partial \chi_\mu}{\partial R_\alpha} \hat{h}_{\mu\nu} + \cdots, \qquad (23)$$

where χ denotes basis functions, and the Pulay correction includes terms from the overlap matrix derivatives and density matrix responses. In practice, for MO-based methods, the force operators incorporate these *via* the gradient of the core Hamiltonian and electron-repulsion integrals in the MO basis, augmented by Pulay contributions from the atomic orbital (AO) to MO transformation.[85]

The derivative Hamiltonian $\partial \hat{H} / \partial R_\alpha$ is thus computed in the MO basis, incorporating electron integrals transformed *via* the MO coefficients from a preceding Hartree–Fock calculation. Specifically, the force operators are derived as[89]

$$\hat{F}_\alpha = \sum_{pq} h_{pq}^\alpha a_p^\dagger a_q + \frac{1}{2} \sum_{pqrs} v_{pqrs}^\alpha a_p^\dagger a_r^\dagger a_s a_q, \qquad (24)$$

where h_{pq}^α and v_{pqrs}^α are the derivative core-Hamiltonian and electron-repulsion integrals, respectively, including Pulay terms for basis set dependence on nuclear positions. In our implementation, we compute the energy gradients using the Hellmann–Feynman theorem by obtaining the derivative of one- and two-electron integrals (including Pulay terms) on a classical computer.

Finally, on a quantum computer, these Fermionic operators are mapped to qubit operators using the Jordan–Wigner transformation, and expectation values are evaluated *via*

$$\langle \psi_k | F_\alpha | \psi_k \rangle = \sum_{i,j} \left(c_j^k\right)^* \cdot c_i^k \left\langle \psi_{VQE} \middle| \hat{E}_j^\dagger A \hat{E}_i \middle| \psi_{VQE} \right\rangle \qquad (25)$$

Quantum computation for molecular Hessian. For surface hopping dynamics, second derivatives of the energy (the Hessian matrix) are crucial for computing vibrational

frequencies and ensuring initial conditions for the propagation.[90–92] The Hessian element for coordinates α and β is

$$H_{\alpha\beta} = \frac{\partial^2 E_k}{\partial R_\alpha \partial R_\beta} = \frac{\partial F_{k,\beta}}{\partial R_\alpha}. \tag{26}$$

Direct analytical computation of the Hessian on a quantum computer is challenging due to the need for higher-order responses. Instead, we could compute the Hessian *via* finite differences of the Hellmann–Feynman gradients:

$$H_{\alpha\beta} \approx \frac{F_{k,\beta}(\mathbf{R} + \varepsilon \mathbf{e}_\alpha) - F_{k,\beta}(\mathbf{R} - \varepsilon \mathbf{e}_\alpha)}{2\varepsilon}. \tag{27}$$

Here, ε should be properly chosen to balance numerical stability and accuracy, minimizing the deviation propagation from the electronic structure solver while capturing curvature.

For each displacement, the molecular geometry is updated, and a new Hartree–Fock calculation provides updated MO coefficients. The calculation of electronic-structure observables is then repeated to obtain the ground-state energy and gradient at the perturbed geometry. The full Hessian is assembled as a $(3N \times 3N)$ matrix (N: the number of atoms).

Time evolution as a surface hopping dynamics

Wigner sampling and Landau–Zener surface hopping dynamics. To propagate the nuclear dynamics while accounting for non-adiabatic effects, we initialize an ensemble of classical trajectories (in the classical physics sense, they were also computed on a classical computer) using Wigner sampling and employ a LZSH algorithm. This combination allows for the incorporation of initial quantum-mechanical nuclear effects and efficient treatment of electronic state transitions without requiring explicit computation of NAC vectors, which is particularly efficient.

Wigner sampling provides a phase-space distribution that approximates the quantum mechanical density for the initial vibrational state, typically the ground state at zero temperature.[93] For a molecule treated as a set of harmonic oscillators derived from the Hessian matrix, the Wigner distribution in normal coordinates $\mathbf{Q}$ and conjugate momenta $\mathbf{P}$ is given by

$$\rho_W(\mathbf{Q}, \mathbf{P}) = \prod_{l=1}^{3N-6} \frac{\alpha_l}{\pi\hbar} \exp\left(-\frac{2}{\hbar\omega_l} \left(\frac{P_l^2}{2} + \frac{1}{2}\omega_l^2 Q_l^2 \right) \right), \tag{28}$$

where ω_l is the frequency of the l-th normal mode and $\alpha_l = \tanh(\hbar\omega_l/2k_BT)$ approaches 1 at $T = 0$ K (the regime considered here).[94] For the ground state, each mode's position Q_l and momentum P_l (scaled by the reduced mass) are independently sampled from Gaussian distributions:

$$Q_l \sim \mathcal{N}\left(0, \frac{\hbar}{2\omega_l}\right), \quad P_l \sim \mathcal{N}\left(0, \frac{\hbar\omega_l}{2}\right). \tag{29}$$

On the classical computer, these normal-mode samples are transformed back into Cartesian coordinates and velocities using the eigenvectors from the Hessian diagonalization, ensuring that the initial ensemble captures zero-point energy

and quantum-mechanical delocalization effects.[93] The sampled trajectories are then propagated on the adiabatic PESs computed *via* VQE and QSE.[72,95] Non-adiabatic transitions are handled *via* the LZSH algorithm, a computationally efficient variant of Tully's FSSH that approximates hopping probabilities using the Landau–Zener formula without needing time-dependent electronic coefficients or NAC.[29] In LZSH, at each time step Δt, for the current active state k and each other state $l \neq k$, the energy gap $\Delta_{kl} = |E_k - E_l|$ is monitored. A hop is considered only if the gap reaches a local minimum (*i.e.*, $\Delta_{kl}(t) > \Delta_{kl}(t - \Delta t)$ and $\Delta_{kl}(t) < \Delta_{kl}(t + \Delta t)$ in a retrospective check), indicating passage through an avoided crossing.[96] The hopping probability from k to l is then given by the Landau–Zener formula for the transition probability:[97,98]

$$P_{k \to l} = \exp\left(-\frac{\pi}{2\hbar} \sqrt{\frac{\Delta_{kl,\min}^3}{|\ddot{\Delta}_{kl,\min}|}} \right), \tag{30}$$

In the implementation, if a random number $\xi \in [0, 1]$ is less than $P_{k \to l}$, a hop occurs, and the velocity is rescaled along the force difference direction to conserve energy; otherwise, the trajectory continues on the current surface.[99]

A challenge of LZSH NAMD is its sensitivity to the choice of the nuclear time step, and it could be less reliable for systems involving more than two electronic states due to oversimplified multi-state interactions. Another critical challenge in LZSH NAMD is the presence of discontinuities in the PESs, which can manifest as artificial local minima in the energy gap when the dynamics reach the far end of the dissociation region where PESs are closely spaced. These artifacts, arising from numerical instabilities in electronic structure solvers (despite high accuracy), lead to erroneous transition probabilities and non-physical dynamics. Hard-coded filtering risks losing valuable information, so, inspired by Jíra *et al.*,[100] we implement a curvature-induced transition protection algorithm tailored for quantum-computing electronic solvers. This approach suppresses spurious transitions from PES fractures over small displacement intervals, relying solely on energy gap information already available in the LZSH procedure (thus requiring no additional electronic-structure calculations) and efficiently refines the dynamics for more physically consistent system evolution (Fig. 2).

Specifically, the algorithm computes a coefficient α that measures the relative change in the second derivative (curvature) of the energy gap Δ_{kl} between the step immediately preceding the detected minimum and the minimum itself:

$$\alpha = \left| \frac{\ddot{\Delta}_{kl,\text{prev}} - \ddot{\Delta}_{kl,\min}}{\ddot{\Delta}_{kl,\min}} \right|, \tag{31}$$

where $\ddot{\Delta}_{kl,\text{prev}}$ and $\ddot{\Delta}_{kl,\min}$ are the curvatures at those respective steps. The purpose of α is to detect whether the minimum is likely an unphysical artifact (*e.g.*, from a discontinuity-induced fracture) rather than a genuine physical feature: a large α indicates an abrupt, suspicious change in the curvature. If $\alpha > c_{\text{block}}$, the hop is blocked as the minimum is deemed discontinuity-induced (*i.e.*, a trivial crossing); if $c_{\text{alert}} \leq \alpha \leq c_{\text{block}}$, a warning is issued (potentially flagging a sharp but physical conical
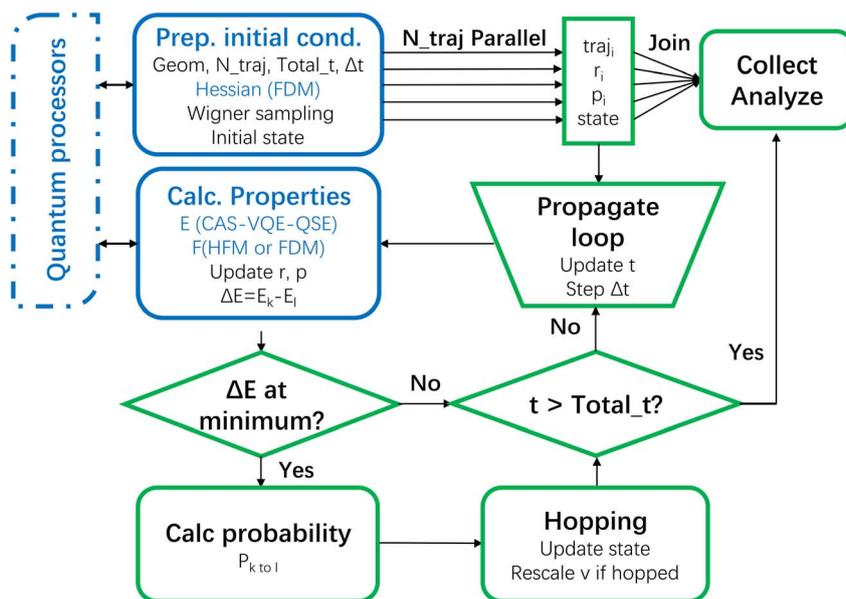
Fig. 2 Work flow of parallel LZSH dynamics (represented by eqn (30)) that co-operates with an on-the-fly quantum-computing electronic-structure property solver.

intersection, akin to a nontrivial crossing); otherwise, the hop proceeds normally. The thresholds c_{alert} and c_{block} are empirical values, summarized as 0.3 and 1.3.[100] This safeguard promotes smooth curvature changes to eliminate spurious crossings arising from numerical artifacts, while preserving physically meaningful ones, thereby improving stability without resorting to hard-coded filters or additional quantum evaluations.

Implementations

Surface-hopping NAMD simulations require repeated execution of electronic structure solvers. In subspace quantum electronic structure solvers, QSE incurs a significant cost, requiring the estimation of $\mathcal{O}(m^8)$ matrix elements, inspired by the serial prototype,[101] noting that the computation of QSE matrix elements in eqn (10) can be parallelized. Each expectation value $\langle \hat{P}_k \rangle$ for Pauli strings in decomposed operators can be estimated independently. We leverage this by performing parallel computations across multiple processors for classical-computing quantum algorithm simulation or real-device quantum computing. On the theoretical level, we exploit the Hermitian feature of QSE matrices to halve the matrix estimation overhead, which is a general strategy. Another optimization applies to systems where dynamics simulations involve only singlet excited-state energies: by selecting operators that commute with $\hat{S}^2$, we achieve a fourfold reduction in the operator count. Furthermore, for specific target states in particular systems, operators with negligible contributions could also be eliminated based on their respective physical nature, enabling problem-specific operator savings.

The surface hopping framework requires a sufficiently large ensemble of trajectories to mitigate statistical noise and accurately capture the underlying physical behavior. Given the resource-intensive nature of quantum algorithm simulators, we leverage the inherent independence of trajectories within the

ensemble to enhance computational efficiency at the engineering level. Each trajectory, initialized from the Wigner distribution by calling the program immigrated from Newton-X-2.4-B06,[102] evolves autonomously under the surface hopping dynamics, allowing for parallelization across multiple processors or computational nodes. In implementation, the initial phase-space points $\mathbf{Q}_l$, and $\mathbf{P}_l$ are assigned to parallel workers. Each worker propagates its assigned subset of trajectories forward in time using the classical-computing integrator on the active surface, interspersed with hop evaluations at each step. The quantum computations for energies E_k and forces F_k are invoked on-demand for each trajectory's current geometry. On the other hand, the curvature-induced hopping correction could maintain computational efficiency. The parameter α in eqn (31) can be obtained using a backward difference of the energy-gap curvatures between the current and previous time steps, eliminating the need for additional wavefunction calculations beyond those already performed in the standard LZSH propagation. The curvature at each time step is computed *via* the central difference of the energy gaps at neighboring steps:

$$\ddot{\Delta}_{kl,t} = \frac{\Delta_{t+1} + \Delta_{t-1} - 2\Delta_t}{(\tau)^2} \tag{32}$$

where τ is the time step size. Note that the energy gap at the trial step $t + 1$ is already calculated in the standard LZSH algorithm to locate the local minimum that triggers surface hopping according to eqn (30). By estimating α using a backward difference of curvatures (relying only on information up to step $t + 1$), we avoid any additional propagation to a hypothetical $t + 2$ step that would otherwise be required for a forward or central difference.

The simulator programs for subspace quantum algorithms are implemented using MindSpore Quantum 0.11.0,[103] Quri-

parts 0.19.0,[104] and Qulacs 0.5.6.[105] To construct our hybrid quantum-classical (both in the physical sense and computational sense) program, we referred to a canonical implementation of the classical AIMD framework in MLatom 3.10 (ref. 106–109) as an initial baseline.

We use PySCF 2.8.0 (ref. 110) to perform the classical-computing reference calculation at the same level corresponding to the quantum-computing solver as the exact solution. All electronic-structure property calculations employ the STO-3G basis set. We pick the UCCSD ansatz[111] for the C_2H_4 use case and k-UpUCCGSD ansatz[112] for the H_3^+ use case respectively. For the VQE parameter optimizer, we use LBFGS.[113,114] In the LZSH program, we pick the time step to be 0.2 fs. On the Wigner sampling for the initial condition preparation, we assume a simple 0 K temperature and δ impulse for excitation, without the filtering using the excitation window. During the NAMD propagation, velocities are rescaled uniformly along their current direction upon a successful hop to compensate for the energy difference between the target and initial electronic states, with the kinetic energy adjusted by the negative of this gap to maintain total energy conservation. A frustrated hop will leave the trajectory at the current electronic state. At the step of curvature-induced hopping correction, given that the instability only occurs at the final stage of dissociation where PESs are very close (see 5d), we set $c_{alert} = 0.3$ and $c_{block} = 0.9$.

Results

In the first subsection, we focus on the 3-orbital-2-electron (CAS(3,2)) space with the charged H_3^+ ion. For this system, we compare PESs along dissociation geometries using the TDA-QSE (as introduced in eqn (9), we denote as "QSE" in the following discussions for simplicity) and operator extended QSE methods (*e.g.* for electron–electron interaction in eqn (17) or other

operators introduced, we denote as "QSE*"), highlighting the systematic accuracy improvement of the QSE* approach. We then evaluate two gradient computation methods (FDM and HFM) under QSE and QSE*, including a comparison of different FDM step lengths. Additionally, we present LZSH-NAMD simulation results using QSE and QSE* as electronic structure solvers, augmented with the curvature-induced hopping correction.

In the second subsection, we would demonstrate adaptability by focusing on a larger molecule C_2H_4. Using hybrid subspace quantum-computing electronic structure solvers, we capture key chemical properties within a selected 2-orbital-2-electron active space (CAS(2,2)): the conical intersection during the 'pyramidalization' process of C_2H_4. We validate high-accuracy quantum-computed PESs along the model path on the quantum simulator, followed by nuclear forces computed *via* the FDM. Finally, we validate our method along a NAMD trajectory.

We compute all the PESs and forces of both H_3^+ and C_2H_4 without the geometric symmetry assumption, which validates the practicality of the electronic structure solvers in NAMD. We selected small basis sets and active spaces to balance computational resources, which necessitate numerous repeated quantum algorithm executions on classical-computing simulators. A larger basis set or active spaces would increase qubit requirements, substantially prolonging VQE and QSE times, escalating overall computation demands despite our parallel optimizations. We opt Hartree as the energy unit which is related to the electronvolt (eV) by the conversion factor of 1 hartree $\approx$ 27.211 eV.

In the remaining subsections, to further evaluate the near-term practical potential, we calculated these observables with a noisy quantum algorithm simulator on a classical computer. As a complement to the long-term potential, we validated some PES calculations for triplet states of H_3^+ and CH_2O,
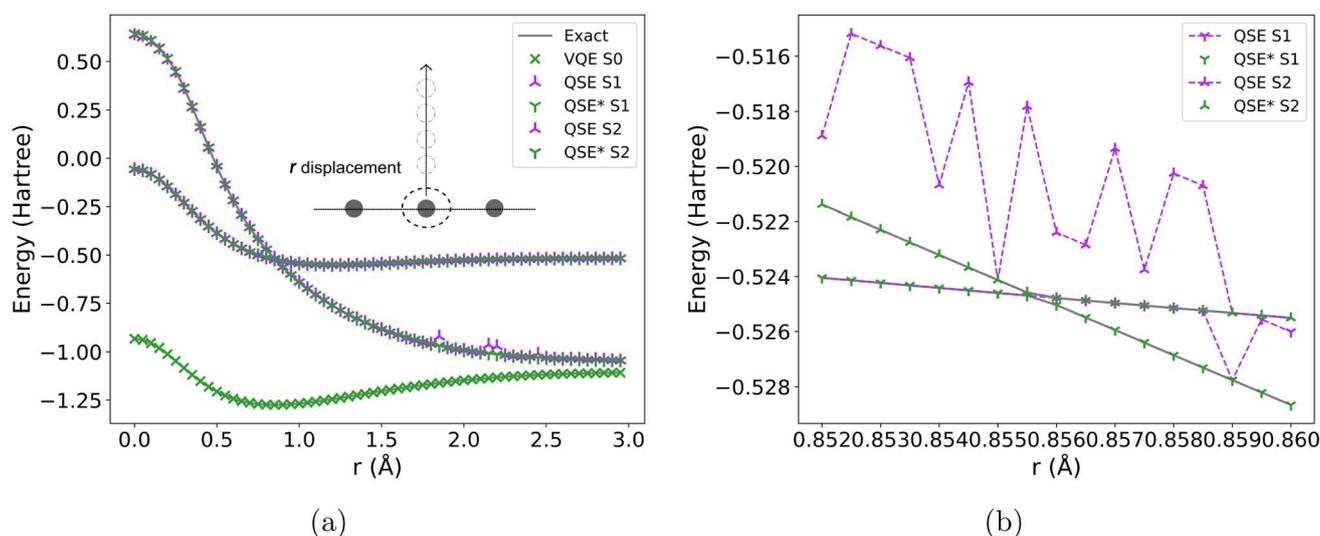

(a)

(b)

Fig. 3 PES result along demonstrative disassociation geometries of H_3^+ in CAS(3,2). Gray lines represent the reference results, purple markers denote the singlet-adapted QSE results, and green markers denote the singlet-adapted QSE* results (augmented with the electron–electron interaction operators that preserve singlet spin multiplicity, as introduced in eqn (17)). (a) PES results compare two methods, with an interval of 0.05 Å between adjacent points. (b) PES results around the intersection region comparing two methods, with an interval of 0.0005 Å.

Table 1 Comparison of PES errors with different interval lengths of different solvers for H_3^+ in CAS(3,2)

ΔE (Hartree)	VQE S_0	QSE* S_1	QSE* S_2	QSE S_1	QSE S_2
0.05 Å interval					
RMSE	9.59×10^{-14}	2.02×10^{-13}	1.49×10^{-14}	9.23×10^{-3}	5.40×10^{-3}
Max error	4.49×10^{-13}	1.34×10^{-12}	8.56×10^{-14}	4.88×10^{-2}	3.14×10^{-2}
MAE	3.87×10^{-14}	6.62×10^{-14}	5.73×10^{-15}	3.35×10^{-3}	2.02×10^{-3}
0.0005 Å interval					
RMSE	6.97×10^{-14}	1.48×10^{-14}	1.50×10^{-14}	1.20×10^{-3}	4.37×10^{-3}
Max error	1.39×10^{-13}	3.31×10^{-14}	4.56×10^{-14}	2.65×10^{-3}	6.77×10^{-3}
MAE	5.12×10^{-14}	8.87×10^{-15}	6.29×10^{-15}	7.22×10^{-4}	3.49×10^{-3}

preliminarily exploring quantum simulations of open-shell systems. Finally, we validate the speedup of our two-level parallelization framework by comparing it to the serial versions.

Use case I: H_3^+ results in CAS(3,2)

The PESs for the H_3^+ cation in its CAS(3,2) space were computed along a dissociation coordinate, where one hydrogen atom is displaced from the equilateral triangular equilibrium geometry. This path encompasses regions of conical intersection between the S_1 and S_2 excited states near $r \approx 0.85$ Å. The singlet adapted VQE (single reference version, as introduced in eqn (7), with the

k-UpUCCGSD ansatz) was employed for the S_0 state, while the singlet adaptation, in both QSE and QSE* variants, was utilized for the S_1 and S_2 states. The QSE* approach, incorporating additional electron–electron interaction operators, thus provides a more accurate description of electron correlation energy for the ion system.

Fig. 3(a) illustrates the PESs over an extended dissociation range (0–3 Å) with an interval of 0.05 Å between adjacent points, comparing the computed energies against exact FCI references (note that for H_3^+, CAS(3,2) already takes all the electrons and orbitals, so here in this case, UCCSD equals FCI). The VQE S_0
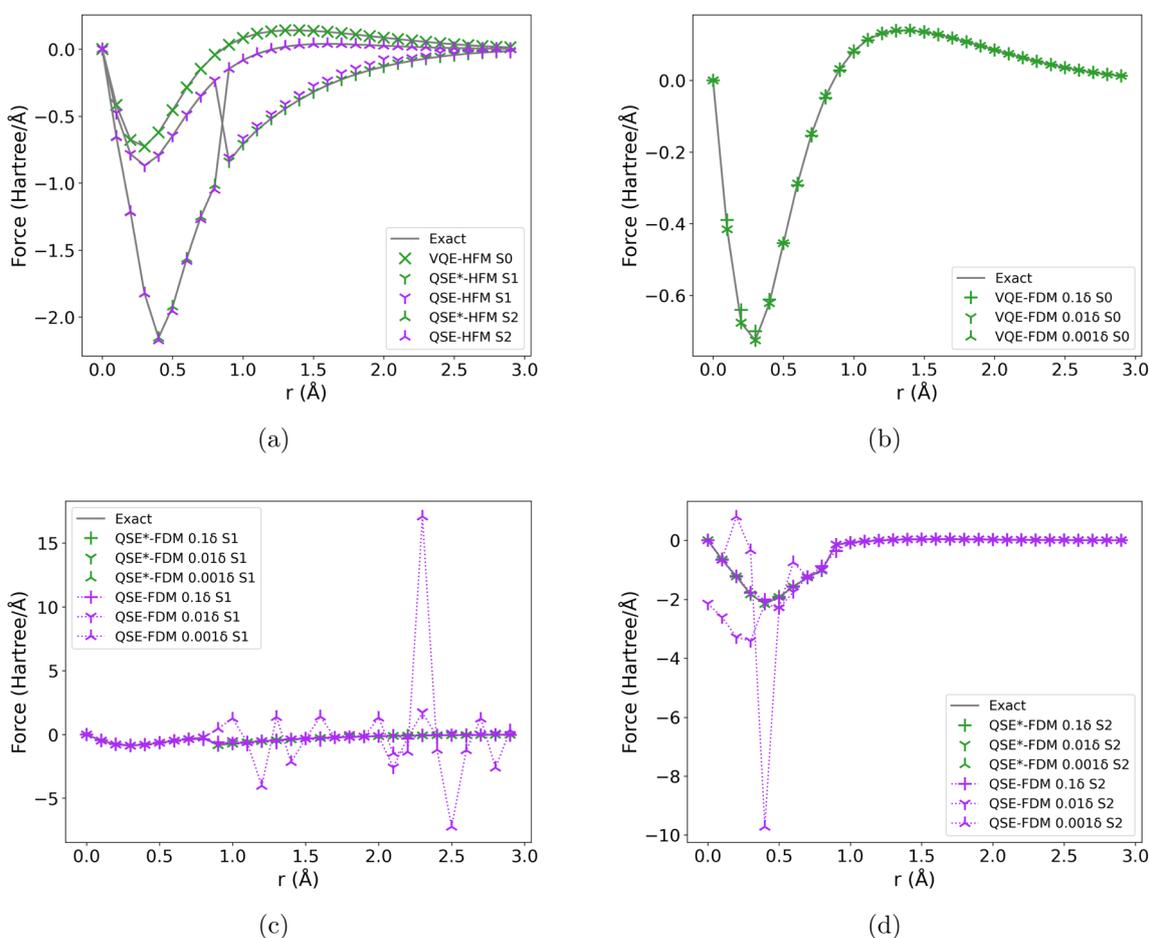

Fig. 4 HFM force results and FDM force results with different step lengths. (a) QSE*-HFM force of each excited state. (b)–(d) FDM force comparison between QSE and QSE* of different FDM step lengths.

Table 2 Comparison of y-axis force error for HFMs in different states (S_0, S_1, and S_2) for the middle H atom of H_3^+

ΔF (Ha Å^{-1})	VQE-HFM S_0	QSE-HFM S_1	QSE*-HFM S_1	QSE-HFM S_2	QSE*-HFM S_2
RMSE	9.53×10^{-8}	1.96×10^{-2}	2.00×10^{-10}	6.59×10^{-3}	0.00
Max error	9.60×10^{-7}	7.97×10^{-2}	2.10×10^{-9}	3.80×10^{-2}	0.00
MAE	2.37×10^{-8}	1.05×10^{-2}	0.00	1.94×10^{-3}	0.00

curve closely tracks the exact ground-state PES, exhibiting a deep potential well at equilibrium bond length, followed by a smooth rise to the dissociation limit. For the excited states, the QSE method yields noticeable deviations, which fail to accurately capture the critical behavior, resulting in oscillations and energy offsets. In contrast, the QSE* method demonstrates good fidelity, with both S_1 and S_2 curves overlaying the exact references across the entire coordinate, including the flat dissociation plateau beyond $r \approx 2.0$ Å.

A magnified view around the conical intersection region (0.852–0.86 Å) is provided in Fig. 3(b), highlighting the PES accuracy even with an interval of 0.0005 Å between adjacent points. The QSE* results reproduce the conical intersection with high precision, whereas the QSE introduces erratic fluctuations indicative of subspace incompleteness due to inadequate selection of operators.

Quantitative energy errors, summarized in Table 1, further underscore these observations. For the PES with an interval of 0.5 Å, VQE achieves root-mean-square error (RMSE) and mean absolute error (MAE) values on the order of 10^{-14} hartree, affirming its robustness for ground-state simulations. The extended method attains comparable sub-microhartree accuracy for S_1 (RMSE $= 2.02 \times 10^{-13}$ hartree) and S_2 (RMSE $= 1.49 \times 10^{-14}$ hartree), with maximum errors below 10^{-11} hartree-orders of magnitude better than the QSE, which incurs RMSEs of 9.23×10^{-3} hartree and 5.40×10^{-3} hartree for S_1 and S_2, respectively. Similar trends persist in the regime with an interval of 0.0005 Å, where QSE* errors remain at the 10^{-14} hartree level, while QSE errors escalate to the millihartree scale (e.g., RMSE $= 4.37 \times 10^{-3}$ hartree for S_2), reflecting its numerical instability near the intersection.

The results presented in Fig. 4, Tables 2 and 3 provide evaluations of the accuracy and robustness of the quantum-computing electronic structure solver for computing nuclear forces. Specifically, we compare the HFM (as in eqn (21)) and FDM (as in eqn (20)) applied within VQE and QSE frameworks, including a QSE* variant. These approaches are assessed against exact analytical forces of reference. Since the calculation of H_3^+ is naturally located on a plane, here on the model trajectory (freezing the positions of the first and third hydrogen atoms), we define the left and right hydrogen atoms as being on the x-axis, and the middle hydrogen atom as starting from the midpoint and moving to one side along the y-axis. We focus on the y-component of the force on the central hydrogen atom as a function of separation distance r.

The HFM results, as illustrated in the noiseless simulations shown in Fig. 4(a), demonstrate that the QSE*-HFM approach yields forces that closely track the exact curve across all examined states (S_0, S_1, and S_2), with minimal deviations even in regions of steep potential gradients or of conical intersection. Quantitative errors of forces in Table 2 underscore this fidelity: for the QSE*-HFM method, RMSEs are on the order of 10^{-10} Ha Å^{-1} or lower for S_1 and S_2, with max error not exceeding 2.1×10^{-9} Ha Å^{-1} and MAE effectively zero within numerical precision. In contrast, QSE-HFM exhibits significantly higher errors for excited states, with RMSE values of 1.96×10^{-2} Ha Å^{-1} for S_1 and 6.59×10^{-3} Ha Å^{-1} for S_2, reflecting challenges in capturing subspace instabilities. For the ground state (S_0), VQE-HFM achieves sub-microhartree accuracy (max error 9.60×10^{-7} Ha Å^{-1}). These findings highlight the applicability of the QSE*, which incorporates additional operators to replenish the

Table 3 Comparison of y-axis force error on the middle H atom of H_3^+ with different FDMs and step lengths

| ΔF (Ha Å^{-1})	VQE-FDM S_0	QSE-FDM S_1	QSE*-FDM S_1	QSE-FDM S_2	QSE*-FDM S_2
$\delta = 0.001$					
RMSE	1.23×10^{-6}	4.74	4.28×10^{-6}	2.81×10^{-1}	4.32×10^{-6}
Max error	9.32×10^{-6}	2.56×10^{1}	3.44×10^{-5}	1.78	3.51×10^{-5}
MAE	3.62×10^{-7}	1.47	1.13×10^{-6}	8.90×10^{-2}	1.24×10^{-6}
$\delta = 0.010$					
RMSE	1.23×10^{-4}	6.09×10^{-1}	4.27×10^{-4}	2.37×10^{-1}	4.31×10^{-4}
Max error	9.33×10^{-4}	2.55	3.41×10^{-3}	1.36	3.47×10^{-3}
MAE	3.62×10^{-5}	2.64×10^{-1}	1.13×10^{-4}	8.04×10^{-2}	1.24×10^{-4}
$\delta = 0.100$					
RMSE	1.27×10^{-2}	2.41×10^{-1}	3.15×10^{-2}	2.32×10^{-1}	3.21×10^{-2}
Max error	9.73×10^{-2}	1.31	2.02×10^{-1}	1.37	2.13×10^{-1}
MAE	3.66×10^{-3}	9.40×10^{-2}	9.95×10^{-3}	8.15×10^{-2}	1.11×10^{-2}
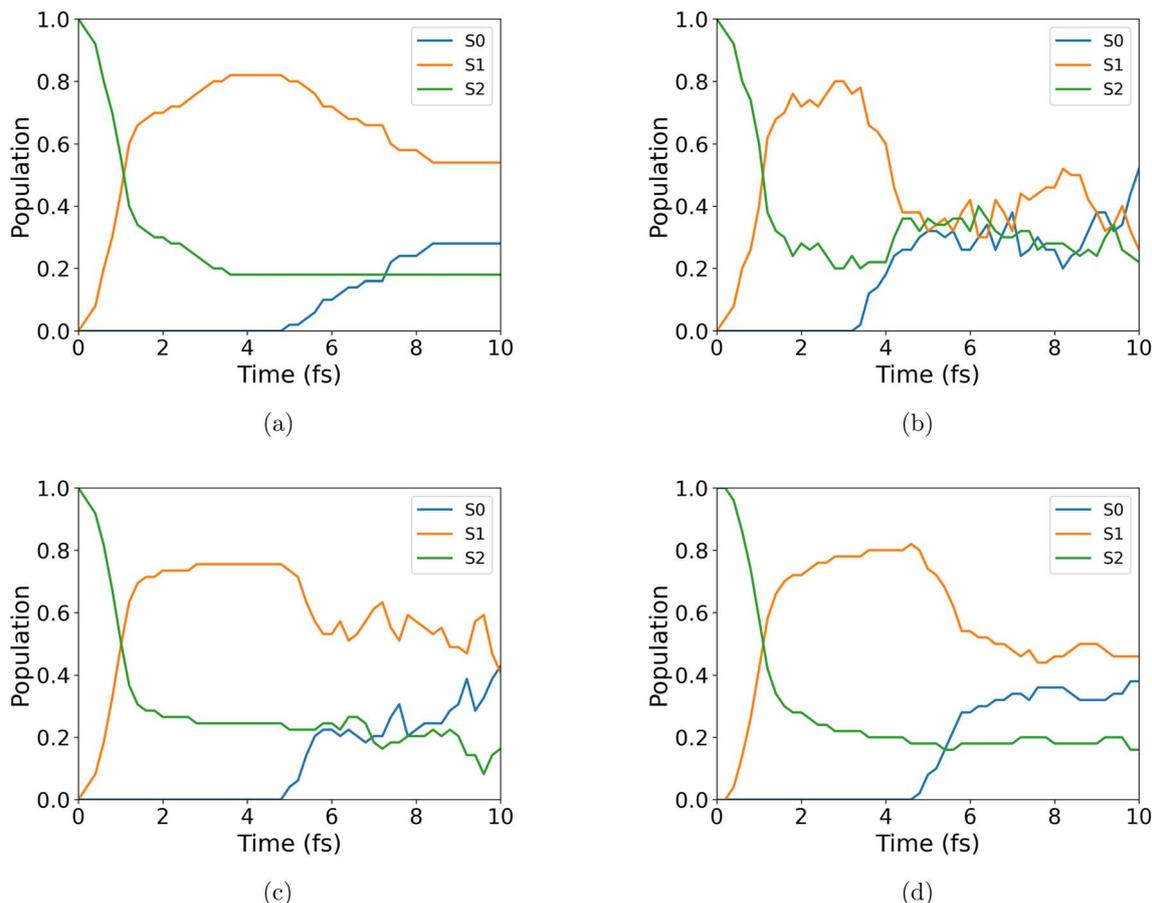
Fig. 5 50-trajectory NAMD population evolution of H_3^+ with different electronic structure solvers and hopping rules. The initial state at S_2. (a) Exact FCI as the electronic structure solver, without curvature-induced hopping correction. (b) VQE-QSE, without curvature-induced hopping correction. (c) VQE-QSE*, without curvature-induced hopping correction. (d) VQE-QSE*, with curvature-induced hopping correction applied.

subspace, thereby enabling the HFM to deliver accurate forces for multi-state dynamics without empirical corrections.

Turning to the FDM in Fig. 4(b)–(d), the force profiles reveal a strong dependence on the finite-difference step size δ. For small δ (e.g., 0.001 Å), both QSE-FDM and QSE*-FDM approximate the exact forces well. Table 3 quantifies this trend: at $\delta = 0.001$ Å, RMSE for VQE-FDM S_0 is 1.23×10^{-6} Ha Å^{-1}, while QSE-FDM S_1 balloons to 4.74 Ha Å^{-1}, indicative of amplified errors. Increasing δ to 0.01 Å and 0.1 Å systematically degrades accuracy across all methods, with RMSE rising by 2 orders of magnitude. Notably, QSE* consistently outperforms QSE in FDM contexts, suggesting that the extended subspace better stabilizes finite differences.

Fig. 5 demonstrates the population evolution during the NAMD simulations of the H_3^+ dissociation process, comparing the performance of the reference classical-computing exact solver with that of quantum computing approaches, including the VQE, QSE and QSE* methods. Fig. 5(a) and (b) illustrates the state populations as a function of time for the reference FCI (left, on the classical computer) and VQE-QSE (right, simulated on the classical computer via a quantum algorithm simulator) methods. In the FCI-driven simulation, which serves as a reference, the state S_1 (blue) depopulates gradually over the initial 4

fs, transferring population primarily to S_1 (orange), which peaks around 5 fs before decaying. After 5 fs, S_0 (blue) receives a smaller but steady population increase. This behavior is indicative of efficient non-adiabatic transfer driven by conical intersections in the H_3^+ PESs, which are well-known to facilitate ultra-fast relaxation in this system.[115] In contrast, the VQE-QSE based simulation exhibits more oscillatory population transfers, with S_1 showing pronounced fluctuations between 2 and 6 fs and S_2 displaying erratic rises and falls, indicative of PES fractures and instability.

The population evolution by the VQE-QSE* with canonical LZSH (Fig. 5(c)) and VQE-QSE* with curvature-induce-corrected LZSH (Fig. 5(d)) is presented. Fig. 5(c) exhibits a smooth transition but instantly turns to oscillations after 6 fs, suggesting sudden emergence of hopping events at the late stage of dissociation, which we ascribe to the discontinuity of PESs with a small displacement interval at the far dissociation plateau, where PESs tend to be close and parallel. In Fig. 5(d), the application of the curvature-driven hopping correction technique (as introduced in eqn (31)) significantly stabilizes the dynamics and makes populations evolve more smoothly, without losing the essential physical picture of the evolution,
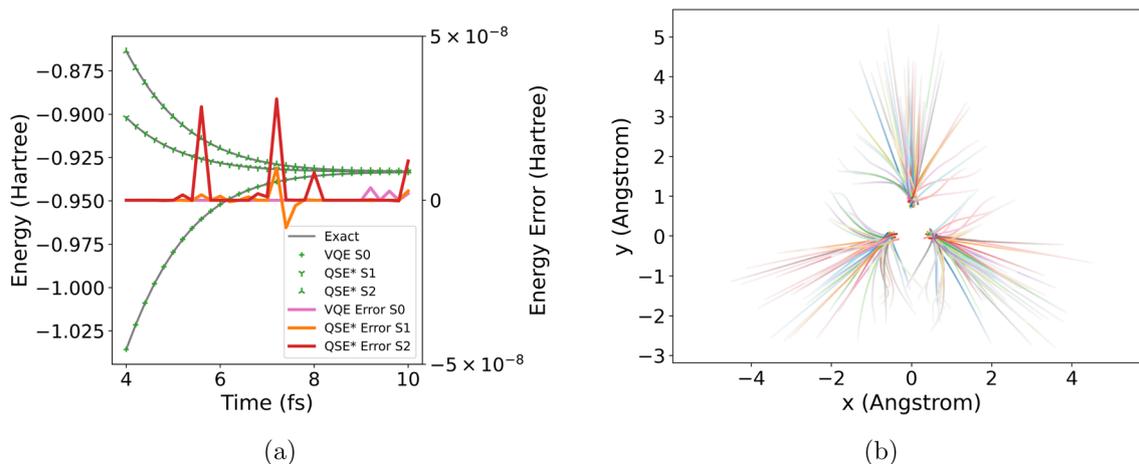
(a)   (b)

Fig. 6 (a) PESs at the end of the dissociation and their instability, taking the view that the displacement interval of geometry is small. (b) Geometry trajectories of the ensemble during the NAMD simulation.

with S_2 smoothly depopulating and S_1 & S_0 stabilizing, closely mimicking the reference population behavior.

In addition, the sharp oscillations observed in Fig. 5(b) and (c) arise not only from the numerical instability of the quantum-computing PES solver but also from an insufficient number of trajectories. In surface-hopping NAMD simulations, a sufficiently large number of trajectories is essential for mitigating statistical noise and achieving reliable ensemble averaging. However, emulating quantum algorithms on classical computers is computationally demanding; thus, to accommodate limited resources, all simulations presented in Fig. 5 employ only 50 trajectories. The erratic fluctuations in panel (b) persist throughout the dynamics, highlighting the inherent instability of the VQE-QSE solver and the inadequacy of the trajectory count. Panel (c), which employs the improved VQE-QSE* method without curvature-induced hopping correction,

exhibits smooth initial behavior but deviates from the exact reference. A similar trend is observed in panel (d) upon application of the curvature correction, where the population evolution does not precisely match the reference. These artifacts primarily originate from the insufficient number of trajectories in the LZSH ensemble.

To quantify the accuracy of the quantum electronic structure solver and to reveal the underlying cause of the late-6 fs oscillation, Fig. 6(a) compares the PESs at late dissociation times from 4 fs onward, where the surfaces S_0, S_1, and S_2 of both reference and VQE-QSE* converge smoothly and closely. Dotted lines depict the absolute energy errors relative to the exact solution, revealing that VQE-QSE* errors remain below 10^{-7} hartree but spike intermittently. Note that the initial guess heritage of VQE during the PES calculation could not fully smoothen such microscopic spikes. These artifacts, though
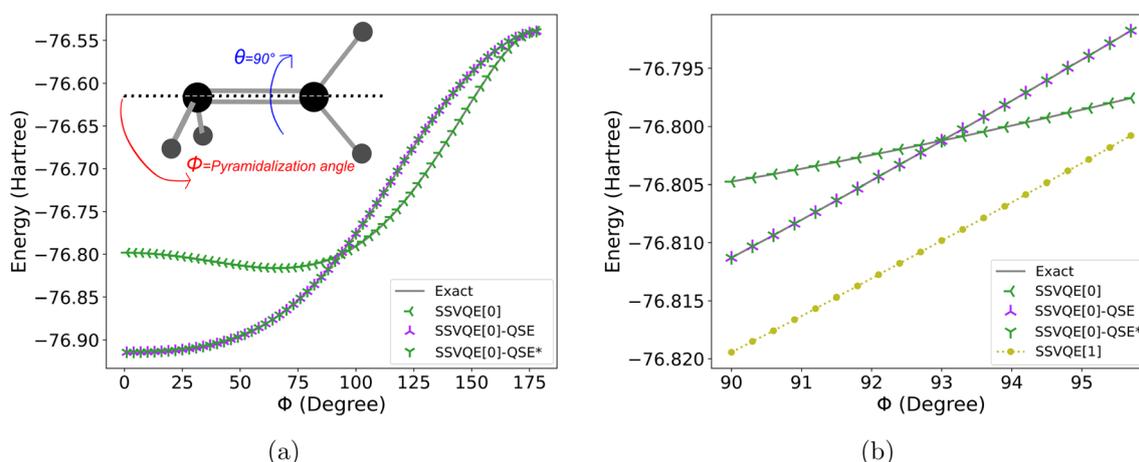

(a)   (b)

Fig. 7 PES results along demonstrative pyramidalization geometries of C_2H_4 in CAS(2,2). Gray lines represent the reference results, while markers denote those obtained *via* quantum electronic structure solvers. (a) PES result with a 3°'s rotation angle interval between data points. SSVQE[0]-QSE indicates the singlet-adapted QSE based on the reference state given by SSVQE with the UCCSD ansatz in the active space, with only single−double excitation operators used to expand subspaces. SSVQE[0]-QSE* indicates the singlet-adapted QSE* with single and double de-excitation operators, expanding subspaces upon the reference state searched by SSVQE. (b) PESs around the conical intersection region with data points' rotation angle interval of 0.3°, also demonstrating comparison between SSVQE-QSE(QSE*) integrated methods and the SSVQE-solo method.

Table 4 Comparison of macroscopic and microscopic C_2H_4 PES errors for different solvers

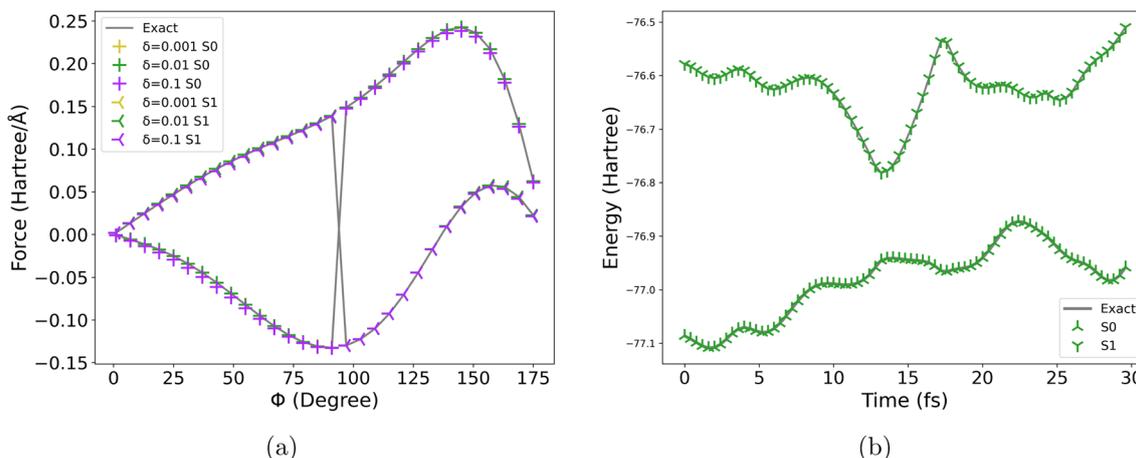| ΔE (Hartree)	SSVQE[0]	SSVQE[0]-QSE	SSVQE[0]-QSE*	SSVQE[1]
3-Degree interval angle				
RMSE	1.033×10^{-13}	7.666×10^{-14}	7.415×10^{-13}	—
Max error	2.416×10^{-13}	1.847×10^{-13}	9.948×10^{-13}	—
MAE	8.266×10^{-14}	5.921×10^{-14}	7.375×10^{-13}	—
0.3-Degree interval angle				
RMSE	1.033×10^{-13}	7.666×10^{-14}	7.415×10^{-13}	8.67×10^{-3}
Max error	2.416×10^{-13}	1.847×10^{-13}	9.948×10^{-13}	9.03×10^{-3}
MAE	8.266×10^{-14}	5.921×10^{-14}	7.375×10^{-13}	8.60×10^{-3}

Fig. 8 Electronic-structure property results necessary for NAMD. (a) x-axis force results along demonstrative pyramidalization geometries of the first carbon atom of C_2H_4 in CAS(2,2). Gray lines represent the reference results, while markers of different colors denote those obtained *via* SSVQE-QSE with different FDM step lengths. (b) PES result by SSVQE-QSE* along a reference LZSH-NAMD trajectory, 30 fs, 75 steps.

small, can induce unphysical hops in regions of near-degeneracy.

The geometric trajectories of the molecular ensemble, visualized in Fig. 6(b), demonstrate the realistic dissociation trajectories in the x–y plane, given by the hopping corrected LZSH-NAMD with the VQE-QSE* solver. The trajectories fan out symmetrically from the central equilibrium geometry, with clusters branching toward positive and negative y-directions. The multi-colored lines indicate temporal evolution, with earlier times near the origin and later dispersion. Atoms in the same trajectory share the same color, whose initial positions and momentum are determined by Wigner sampling.

Use case II: C_2H_4 results in CAS(2,2)

To assess the adaptability of the subspace-based quantum electronic structure solvers in capturing the PESs, we examine the pyramidalization pathway of C_2H_4 within the complete active space (CAS(2,2)) framework, which encompasses the π and π^* orbitals. Fig. 7(a) illustrates the PES with a large displacement interval along the pyramidalization angle ϕ, comparing the exact diagonalization results (gray lines) with SSVQE[0]-QSE and SSVQE[0]-QSE*.

Quantitative energy errors for these solvers are summarized in Table 4. Among PESs with an interval degree of 3 and 0.3

between data points, all the hybrid subspace-based solvers reached sub-microhartree accuracy. Compared to the CAS(3,2) ionic system examined in the preceding section, the current system features a smaller active space, enabling QSE to exhibit high accuracy in the exemplified regime as well. This underscores the utility of QSE in certain scenarios. However, the QSE* demonstrates slightly lower fidelity because expanding

Table 5 Comparison of force errors on the first carbon atom of C_2H_4 with different FDM steps

ΔF (Hartree Angstrom^{-1})	S_0	S_1
$\delta = 0.001$ hartree		
RMSE	3.740×10^{-7}	2.187×10^{-7}
Max error	6.312×10^{-7}	4.209×10^{-7}
Mean absolute error	3.238×10^{-7}	1.946×10^{-7}
$\delta = 0.010$ hartree		
RMSE	3.29165×10^{-5}	1.78885×10^{-5}
Max error	5.12144×10^{-5}	2.91406×10^{-5}
Mean absolute error	2.94293×10^{-5}	1.48558×10^{-5}
$\delta = 0.100$ hartree		
RMSE	3.2648329×10^{-3}	1.7893454×10^{-3}
Max error	5.0488511×10^{-3}	2.9237422×10^{-3}
Mean absolute error	2.9277802×10^{-3}	1.4836350×10^{-3}

Table 6 Comparison of PES errors for C_2H_4 along the NAMD trajectory

ΔE (Hartree)	S_0	S_1
RMSE	1.57×10^{-13}	2.5747180×10^{-8}
Max error	7.53×10^{-13}	$1.06571761 \times 10^{-7}$
Mean absolute error	1.12×10^{-13}	1.1482544×10^{-8}

Table 7 Comparison of noisy PES errors of H_3^+

ΔE (Hartree)	S_0	S_1	S_2
RMSE	3.556×10^{-2}	2.240×10^{-2}	1.409×10^{-2}
Max error	7.966×10^{-2}	5.650×10^{-2}	3.961×10^{-2}
MAE	3.092×10^{-2}	1.917×10^{-2}	9.822×10^{-3}

subspaces with extra operators would introduce more linear independence, which leads to a larger condition number of overlapping matrix S, affecting numerical stability.

Here, we present the results prior to energy ordering of the states. Unlike the conventional scenario, where VQE is used to search the ground state followed by QSE to obtain excited states, here, SSVQE (as introduced in eqn (8)) yields the higher-energy V state[116] in the region before the conical intersection. In contrast, QSE, by expanding the subspace, expands the lower-energy N state in this region. Furthermore, SSVQE demonstrates robust state-tracking capabilities. After the conical intersection, SSVQE continues to track the V state (which now becomes the

ground state), while QSE, leveraging the reference state from this region, accurately extends to the higher-energy excited state.

A more detailed examination of the region of PESs with an interval of 0.3° around the conical intersection is provided in Fig. 7(b), where we compare the energy of the N-state and V-state directly from SSVQE. The hybrid subspace-based solvers maintain high fidelity to the exact curves, with correct transitions through the conical intersection region. In contrast, the SSVQE-solo results deviate noticeably. This behavior indicates that where the weighted sum of energies from orthogonal references (eqn (8)) is insufficient to resolve all subspaces without additional constraints, it requires a more advanced SSVQE extension or other methods.
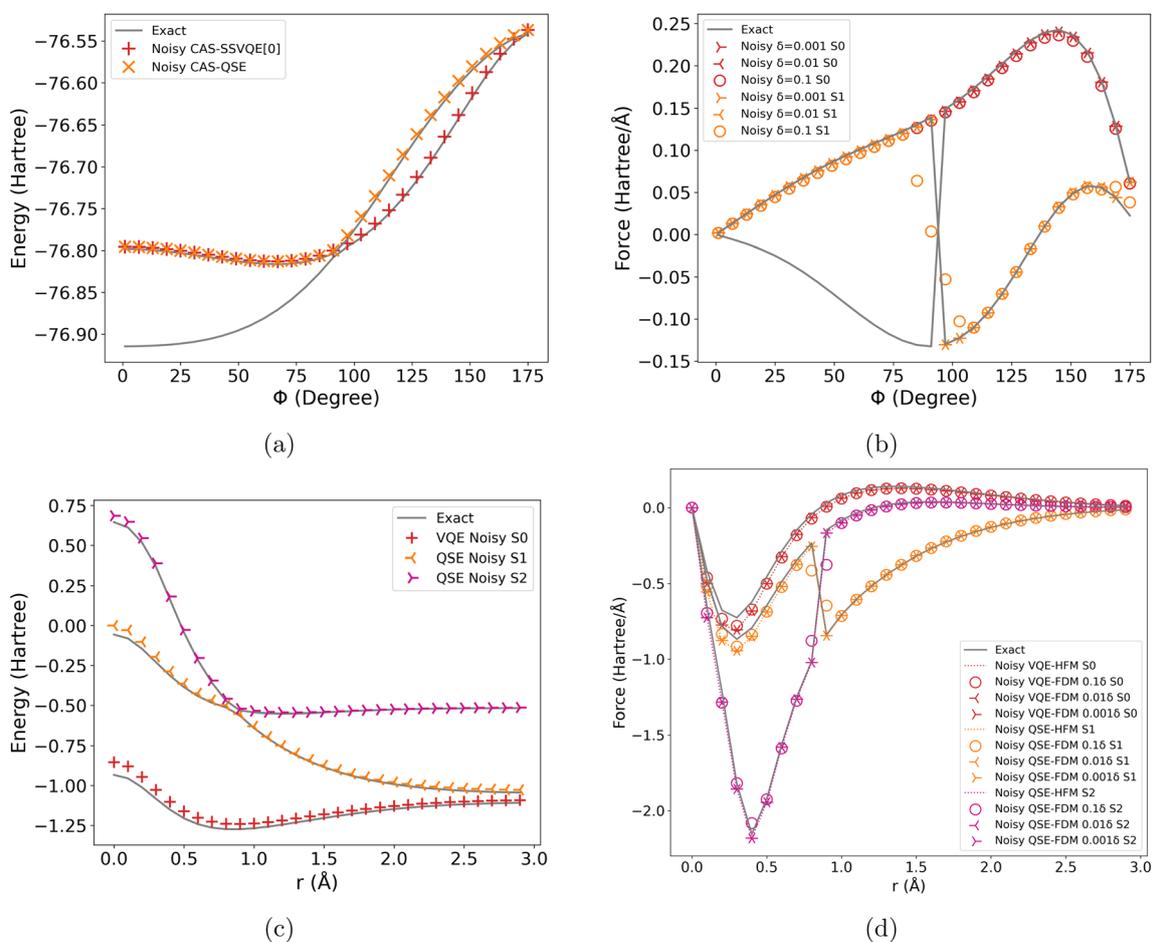

Fig. 9 Noisy PES and force results of C_2H_4 in CAS(2,2) and H_3^+ in CAS(3,2). Gray lines represent the reference results, while markers denote those obtained via a noisy quantum algorithm simulator on a classical computer. (a) Noisy PES result of C_2H_4. (b) Noisy FDM force result with different step lengths of C_2H_4. (c) Noisy PES result of H_3^+. (d) Noisy FDM and HFM force results with different step lengths of H_3^+. We add depolarization noise with a probability of 0.01 for the double-qubit gate and 0.001 for the single-qubit gate.
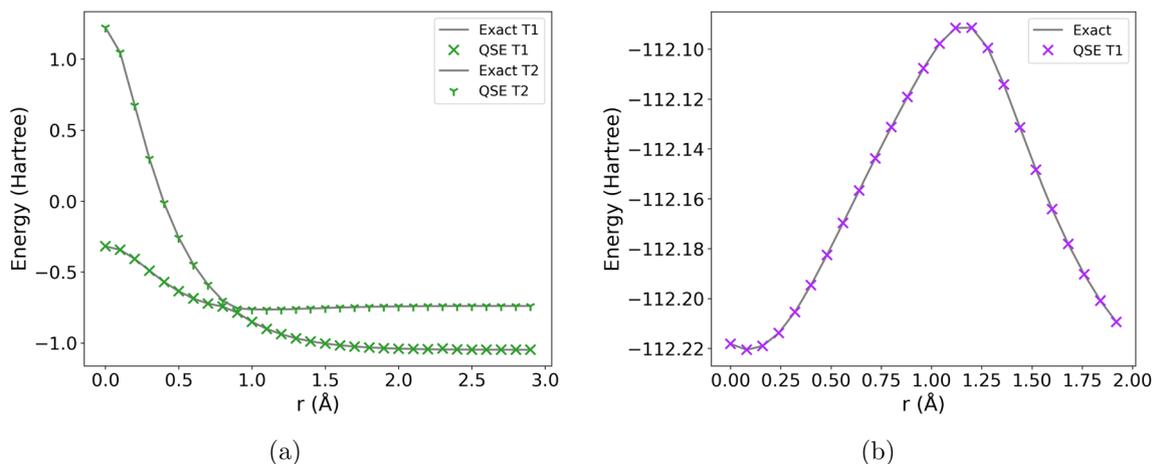
Fig. 10 Triplet PES results by QSE. (a) CAS(3,2) T1 and T2 of H_3^+ and (b) CAS(3,2) T1 of CH_2O.

The force calculations along the pyramidalization coordinate of the first carbon atom in C_2H_4 within the CAS(2,2) active space reveal the efficacy of the FDM integrated with quantum electronic structure solvers for excited-state properties. As illustrated in Fig. 8 and Table 5 taking the x-axis for demonstration, the reference exact forces (gray lines) are closely reproduced by both the hybrid subspace-based solvers, with deviations becoming more pronounced at larger FDM step lengths (δ). For $\delta = 0.001$, the computed forces overlay nearly identically with the exact profile across the full range of dihedral angles, capturing changes around the conical intersection. In contrast, larger steps ($\delta = 0.01$ and 0.1) introduce systematic errors, manifesting as offsets.

Complementing the static analysis, Fig. 8(b) and Table 6 present the SSVQE-QSE* PESs along the geometry of a LZSH-NAMD reference trajectory, capturing the temporal evolution of S_0 and S_1 energies in 30 fs. However, along this realistic trajectory, QSE fails largely at many geometries; thus only QSE* results are presented. The SSVQE-QSE* energies for S_0 and S_1 faithfully reproduce the result using the exact reference electronic solver.

Noisy results

In Fig. 9 and Table 7 we demonstrate the PES and nuclear forces of two chemical systems C_2H_4 and H_3^+, under noisy quantum simulation conditions. For C_2H_4, in the range before the conical intersection, the noisy QSE fails to expand the N-state based on the V-state searched by noisy SSVQE. This revealed that quantum noise significantly impacts the cooperation of the hybrid subspace-based quantum solver, preventing it from reaching the target states.

In contrast, the H_3^+ system exhibits a smoother response to noise, manifesting as a consistent offset in the PES and nuclear forces. Notably, QSE calculations based on noisy ground states yielded excited-state deviations smaller than those of the corresponding noisy ground states. This behavior is attributed to the error mitigation capabilities inherent in the QSE framework (as introduced in the previous section), showing its robustness in noisy environments.

Triplet results

To further explore the utility of the subspace quantum-computing electronic structure solver, we evaluated its performance in computing triplet state energies, as shown in Fig. 10 and Table 8. For CH_2O, the CAS(3,2) active space consisted of the three Hartree–Fock canonical orbitals straddling the Fermi level. Here, the QSE consistently yields three degenerate or near-degenerate energy values for triplet states. We explored two strategies for processing these values: averaging the three energies or selecting the median value, with the latter often proving more accurate. These findings demonstrate QSE's potential for investigating more sophisticated excited-state dynamics in future studies.

Computational resource analysis

To quantify the impact of our parallelization strategies on computational efficiency, we present benchmark results from executing the QSE algorithm *via* a quantum algorithm simulator on a classical computer, focusing on wall-clock times for key components of the excited-state dynamics simulation. Fig. 11(a) illustrates the CPU times required for ground-state energy evaluations using VQE with UCCSD (1a: 4.86 s) and its noisy variant (1b: 72.42 s), excited-state subspace diagonalizations *via* various QSE implementations (2a–2g), and force computations employing FDM or HFM approaches (3a–3d).

Table 8 Comparison of QSE T1 and T2 ΔE errors (Hartree) for H_3^+ and CH_2O

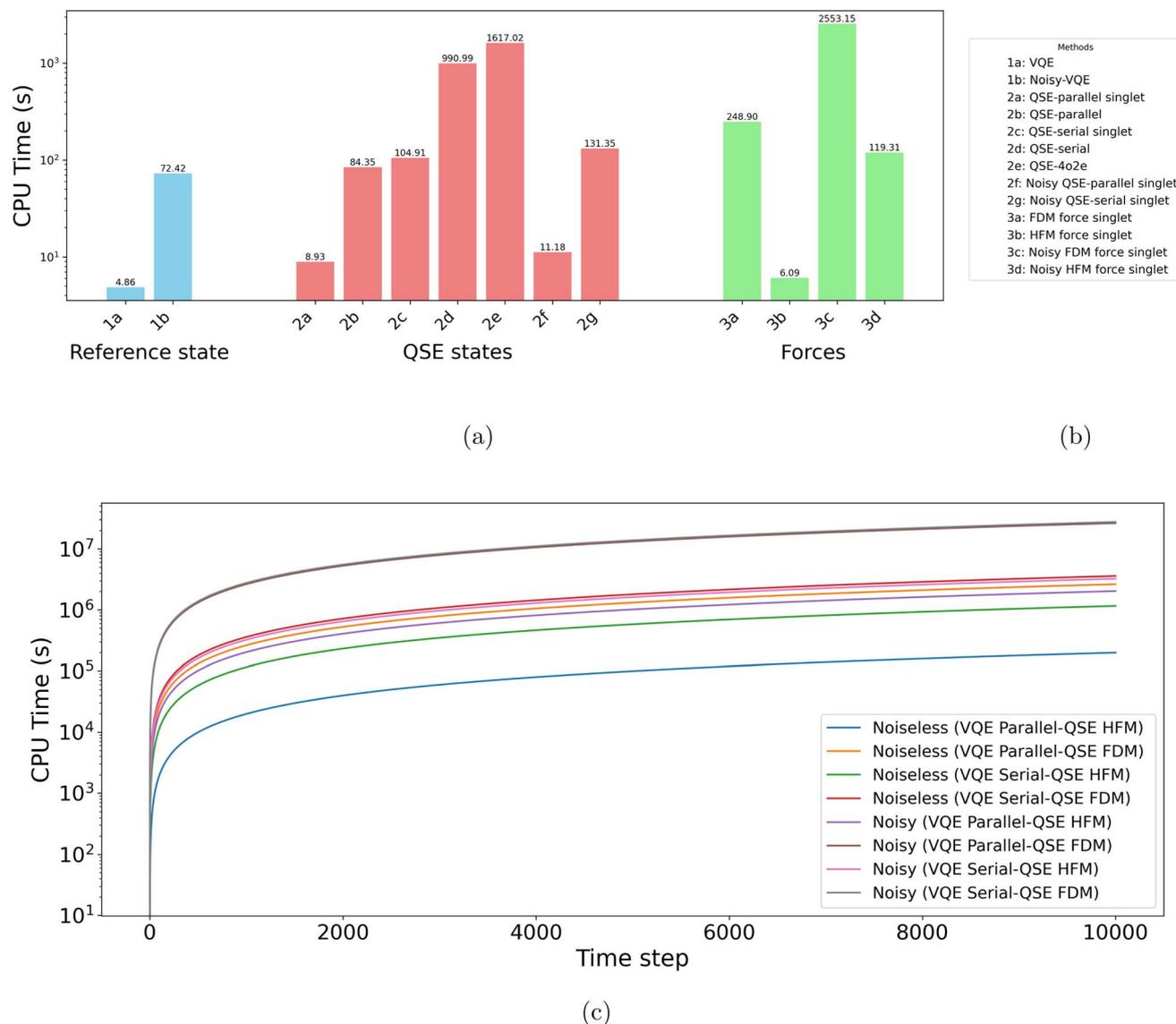| ΔE (Hartree)	T1 average	T2 average	T1 middle	T2 middle
H_3^+				
RMSE	1.14×10^{-3}	1.83×10^{-4}	0.0	0.0
Max error	5.65×10^{-3}	9.99×10^{-4}	0.0	0.0
MAE	4.19×10^{-4}	3.75×10^{-5}	0.0	0.0
CH_2O				
RMSE	6.80×10^{-8}	—	0.0	—
Max error	3.40×10^{-7}	—	0.0	—
MAE	1.36×10^{-8}	—	0.0	—

Fig. 11 CPU time comparison and estimation of the simulation. Except for 2e cases in plot (a), all the QSE implementations are tested on CAS(3,2). (a) CPU time of different QSE implementations on calculating energies and forces. (b) Legend for plot (a). (c) CPU time estimation for classical–computing simulation of different quantum–computing LZSH parallel strategies.

Notably, the parallelized QSE implementations demonstrate substantial speedups over their serial counterparts. For the spin-adapted singlet variant, the parallel QSE (2a: 8.93 s) achieves approximately a 12-fold reduction compared to the serial QSE (2c: 104.91 s), attributable to the concurrent evaluation of expectation values for the independent Pauli strings in the H and S matrices (eqn. (10)). Similarly, for the triplet QSE, parallelization (2b: 84.35 s) yields a comparable $12\times$ speedup relative to the serial case (2d: 990.99 s). The CAS(4,2) (4o2e) QSE-triplet (2e: 1617.02 s), which incorporates excitation operators, incurs additional overhead due to the increased subspace dimension, highlighting the trade-off between accuracy and efficiency in a larger subspace. Under noisy conditions, emulating realistic quantum hardware errors, the parallel singlet QSE (2f: 131.35 s) remains efficient. For QSE*, since we have expanded more operators and conducted parallel

estimation on these operators, the acceleration effect will be more significant if there is sufficient hardware.

At the force computation level, the HFM approach (3b: 6.09 s) outperforms the FDM (3a: 248.90 s) by $41\times$ in the noiseless regime, reflecting the lower measurement demands of direct derivative evaluations compared to the FDM. Noise channel simulation amplifies this disparity, with the noisy FDM (3c: 2553.15 s) being $21\times$ slower than the noisy HFM (3d: 119.31 s).

Extending to full trajectory propagation, Fig. 11(c) depicts the cumulative computation time as a function of time steps for a representative non-adiabatic dynamics simulation under LZSH, comparing noiseless and noisy scenarios with parallel *versus* serial QSE integrated into VQE for ground-state preparation, alongside HFM or FDM for forces. The parallel QSE configurations consistently exhibit shallower slopes, indicating reduced per-step overhead. For instance, the noiseless VQE with

parallel-QSE and HFM (blue line) accumulates 10^5 s by 10 000 steps, whereas the serial-QSE equivalent (green line) approaches 10^6 s, a $10\times$ difference arising from the distributed measurement strategy. This gap widens in noisy emulations, where parallel-QSE with the FDM (purple line) remains below 10^7 s, while serial-QSE with the FDM (magenta line) exceeds it, emphasizing the robustness of parallelization to noise channel computation. The HFM variants are generally preferred over their FDM counterparts within each category, aligning with the single-point benchmarks, though the asymptotic scaling remains dominated by the QSE matrix construction.

Beyond the per-trajectory level, our trajectory-level parallelization exploits the parallel nature of the ensemble, distributing independent Wigner-sampled trajectories across computational nodes. While not explicitly benchmarked here due to hardware constraints, scaling analyses suggest near-linear speedups with the number of processors, limited only by load balancing in asynchronous hop events. Collectively, these optimizations reduce overall simulation wall times by 1–2 orders of magnitude for typical photochemistry applications with 10–100 trajectories and active spaces of 4–8 orbitals, paving the way for efficient quantum-classical hybrid simulations.

While our benchmarks focus on validating the efficiency gains from parallelization (*via* classical-computing emulations of quantum algorithms), it is important to contextualize these results against traditional classical computational chemistry software. At present, simulations of quantum algorithms on a classical computer are substantially slower than well-optimized classical programs (*e.g.*, those implemented in C++/Fortran with extensive algorithmic refinements), stemming from the emulation's need to mimic quantum operations through matrix-vector computations (or matrix–matrix computation for a noisy quantum circuit) with limited optimizations to preserve universality. Moreover, current quantum hardware lacks the necessary fidelity for high-precision electronic structure calculations, precluding direct comparisons of real quantum runtimes.

In terms of user experience, classical software programs (*e.g.* Pyscf,[110] Molpro,[117] Psi4,[118] *etc.*) offer seamless access to a broad array of properties beyond energies, such as spin expectation values (S^2) and configuration interaction coefficients facilitated by storing the full wavefunction in classical memory for efficient post-processing. Quantum approaches, by contrast, require explicit measurements for each desired observable—*e.g.*, additional shots for S^2 *via* spin operators—and accessing configuration interaction coefficients demands quantum state tomography to retrieve all 2^n amplitudes (n being the number of spin orbitals), which is exponentially challenging and resource-intensive. Thus, while quantum methods hold promise for scaling to larger systems, classical quantum chemistry software currently provides a more convenient and comprehensive workflow.

Conclusion

In this work, we have developed an efficient quantum computational framework for NAMD, in which parallelization is supported for both high-precision PES calculation and quantum-algorithm adapted LZSH trajectory simulation. Our approach integrates the CAS framework with VQE and its subspace variant SSVQE, to adaptably prepare reference states. Additionally, we incorporate QSE and its extended variant QSE* for accurate excited-state calculations. Beyond energy spectrum computation, our method enables the calculation of nuclear forces by interfacing quantum-computing PES solvers with the HFM and FDM. Another advancement is the seamless integration of quantum algorithms with the LZSH framework, augmented by curvature-induced hopping corrections to mitigate PES fluctuations at dissociation limits.

Numerical benchmarks on H_3^+, C_2H_4, and CH_2O demonstrate sub-microhartree accuracy on PESs by our hybrid subspace quantum-computing electronic structure solvers. By validating the problem-tailored QSE operator extension, we enhance the adaptability of our approach across those diverse chemical systems. The incorporation of quantum-computing electronic structure solvers and curvature-driven hopping correction in LZSH significantly improves the robustness of NAMD simulations while preserving efficiency, as evidenced by comparisons with exact reference results. Furthermore, computational resource analysis shows that our two-level parallelization framework delivers substantial computational speedups, fully transferable to a real quantum computer, without compromising precision.

This work advances quantum computational NAMD by addressing critical bottlenecks in efficiency and robustness at both the trajectory level and electronic structure levels, while enhancing the adaptability and precision of PES calculation. These advancements pave the way for exploring non-adiabatic effects in polyatomic molecules beyond classical computational limits while facilitating the practical utility of quantum computing. However, challenges persist, including the systematic handling of S matrix ill-conditioning in QSE, ansatz expressivity in VQE, and integration with advanced infrastructures to handle quantum noise. Future efforts will focus on integrating orbital optimization techniques, such as the complete active space self-consistent field (CASSCF) method, developing systematic QSE extension strategies, and exploring the embedding of quantum computing in other NAMD frameworks.

Conflicts of interest

There are no conflicts to declare.

Data availability

The data supporting this article have been included as part of the supplementary information (SI) of this article. Data and scripts for this paper, including the PES, forces and NAMD initial conditions, are available at Zenodo at: https://doi.org/10.5281/zenodo.17865112. The code utilized in this study is available in the project Gitee repository: https://gitee.com/mindspore/mindquantum/new/research/paper_with_code/Efficient_Quantum_Simulation_of_Non-Adiabatic_

Molecular_Dynamics_with_Precise_Electronic_Structure. Supplementary information is available. See DOI: https://doi.org/10.1039/d5dd00433k.

Acknowledgements

References

1 O. V. Prezhdo, others Efficient Modeling of Quantum Dynamics of Charge Carriers in Materials Using Short Nonequilibrium Molecular Dynamics, *J. Phys. Chem. Lett.*, 2023, **14**, 8289–8295.

2 L. González and P. Marquetand, The Quest to Simulate Excited-State Dynamics of Transition Metal Complexes, *JACS Au*, 2021, **1**, 1130–1150.

3 C. Li and G. A. Voth, Using Constrained Density Functional Theory to Track Proton Transfers and to Sample Their Associated Free Energy Surface, *J. Chem. Theory Comput.*, 2021, **17**, 5759–5765.

4 B. F. E. Curchod and T. J. Mart'inez, Ab Initio Nonadiabatic Quantum Molecular Dynamics, *Chem. Rev.*, 2018, **118**, 3305–3336.

5 S. Mai and L. Gonz'alez, Molecular Photochemistry: Recent Developments in Theory, *Angew. Chem., Int. Ed.*, 2020, **59**, 16832–16846.

6 M. Born and J. R. Oppenheimer, Zur Quantentheorie der Molekeln, *Ann. Phys.*, 1927, **389**, 457–484.

7 R. N. Barnett and U. Landman, Born-Oppenheimer molecular-dynamics simulations of finite systems: Structure and dynamics of $(H_2O)_2$, *Phys. Rev. B: Condens. Matter Mater. Phys.*, 1993, **48**, 2081–2097.

8 T. D. Kühne, M. Krack, F. R. Mohamed and M. Parrinello, Efficient and Accurate Car-Parrinello-like Approach to Born-Oppenheimer Molecular Dynamics, *Phys. Rev. Lett.*, 2007, **98**, 066401.

9 A. M. N. Niklasson, Extended Born-Oppenheimer Molecular Dynamics, *Phys. Rev. Lett.*, 2008, **100**, 123004.

10 L. X. Chen, Probing Transient Molecular Structures in Photochemical Processes Using Laser-Initiated Time-Resolved X-Ray Absorption Spectroscopy, *Chem. Rev.*, 2004, **104**, 2665–2692.

11 B. F. E. Curchod and I. Tavernelli, Ultrafast Spectroscopy of Photoactive Molecular Systems from First Principles: Where We Stand Today and Where We Are Going, *J. Phys. Chem. Lett.*, 2020, **11**, 6271–6281.

12 E. Romero, R. Augulis, V. I. Novoderezhkin, M. Ferretti, J. Thieme, D. Zigmantas and R. van Grondelle, Quantum Coherence in Photosynthesis for Efficient Solar-Energy Conversion, *Nat. Phys.*, 2014, **10**, 676–682.

13 D. R. Weinberg, C. J. Gagliardi, J. F. Hull, C. F. Murphy, C. A. Kent, B. C. Westlake, J. Rosenthal, G. W. Coates and T. J. Meyer, Proton-Coupled Electron Transfer, *Chem. Rev.*, 2012, **112**, 4016–4093.

14 M. H. V. Huynh and T. J. Meyer, Proton-Coupled Electron Transfer, *Chem. Rev.*, 2007, **107**, 5004–5064.

15 S. Hammes-Schiffer, Proton-Coupled Electron Flow in Protein Redox Machines, *Chem. Rev.*, 2010, **110**, 6939–6960.

16 W. Domcke, D. R. Yarkony and H. Köppel, *Conical Intersections: Electronic Structure, Dynamics & Spectroscopy*, World Scientific, Singapore, 2004, vol. 15.

17 G. A. Worth and L. S. Cederbaum, Beyond Born-Oppenheimer: Molecular Dynamics Through a Conical Intersection, *Annu. Rev. Phys. Chem.*, 2004, **55**, 127–158.

18 B. G. Levine and T. J. Martínez, Isomerization Through Conical Intersections, *Annu. Rev. Phys. Chem.*, 2007, **58**, 613–634.

19 S. Matsika, *Reviews in Computational Chemistry*, John Wiley & Sons, Ltd, Hoboken, NJ, 2007, pp. 83–124.

20 S. Matsika and P. Krause, Nonadiabatic Events and Conical Intersections, *Annu. Rev. Phys. Chem.*, 2011, **62**, 621–643.

21 B. G. Levine, M. P. Esch, B. S. Fales, D. T. Hardwick, W.-T. Peng and Y. Shu, Conical Intersections at the Nanoscale: Molecular Ideas for Materials, *Annu. Rev. Phys. Chem.*, 2019, **70**, 21–43.

22 L. Shen, B. Xie, Z. Li, L. Liu, G. Cui and W.-H. Fang, Role of Multistate Intersections in Photochemistry, *J. Phys. Chem. Lett.*, 2020, **11**, 8490–8501.

23 S. Matsika, Electronic Structure Methods for the Description of Nonadiabatic Effects and Conical Intersections, *Chem. Rev.*, 2021, **121**, 9407–9449.

24 M. Beck, A. Jäckle, G. Worth and H.-D. Meyer, The multiconfiguration time-dependent Hartree (MCTDH) method: a highly efficient algorithm for propagating wavepackets, *Phys. Rep.*, 2000, **324**, 1–105.

25 L. L. E. Cigrang, *et al.*, Roadmap for Molecular Benchmarks in Nonadiabatic Dynamics, *J. Phys. Chem. A*, 2025, **129**, 7023–7050.

26 X. Li, J. C. Tully, H. B. Schlegel and M. J. Frisch, Ab initio Ehrenfest dynamics, *J. Chem. Phys.*, 2005, **123**, 084106.

27 M. Ben-Nun, J. Quenneville and T. J. Martínez, Ab Initio Multiple Spawning: Photochemistry from First Principles Quantum Molecular Dynamics, *J. Phys. Chem. A*, 2000, **104**, 5161–5175.

28 R. K. Preston and J. C. Tully, Trajectory Surface Hopping Approach to Nonadiabatic Molecular Collisions: The Reaction of H+ with D2, *J. Chem. Phys.*, 1971, **55**, 562–572.

29 J. C. Tully, Molecular dynamics with electronic transitions, *J. Chem. Phys.*, 1990, **93**, 1061–1071, introduces the fewest switches surface hopping (FSSH) algorithm, which LZSH builds upon, providing a framework for nonadiabatic dynamics.

30 A. K. Belyaev, C. Lasser and G. Trigila, Landau–Zener type surface hopping algorithms, *J. Chem. Phys.*, 2014, **140**, 224108.

31 C. Zhu and H. Nakamura, Theory of nonadiabatic transition for general two-state curve crossing problems.

I. Nonadiabatic tunneling case, *J. Chem. Phys.*, 1994, **101**, 10630–10647.

32 C. Zhu, H. Kamisaka and H. Nakamura, New implementation of the trajectory surface hopping method with use of the Zhu–Nakamura theory, *J. Chem. Phys.*, 2001, **115**, 3031–3044.

33 C. Zhu, H. Kamisaka and H. Nakamura, New implementation of the trajectory surface hopping method with use of the Zhu–Nakamura theory. II. Application to the charge transfer processes in the 3D DH_2^+ system, *J. Chem. Phys.*, 2002, **116**, 3234–3243.

34 Y. Shu, L. Zhang, X. Chen, S. Sun, Y. Huang and D. G. Truhlar, Nonadiabatic Dynamics Algorithms with Only Potential Energies and Gradients: Curvature-Driven Coherent Switching with Decay of Mixing and Curvature-Driven Trajectory Surface Hopping, *J. Chem. Theory Comput.*, 2022, **18**, 1320–1328.

35 X. Zhao, Y. Shu, L. Zhang, X. Xu and D. G. Truhlar, Direct Nonadiabatic Dynamics of Ammonia with Curvature-Driven Coherent Switching with Decay of Mixing and with Fewest Switches with Time Uncertainty: An Illustration of Population Leaking in Trajectory Surface Hopping Due to Frustrated Hops, *J. Chem. Theory Comput.*, 2023, **19**, 1672–1685.

36 X. Zhao, I. C. D. Merritt, R. Lei, Y. Shu, D. Jacquemin, L. Zhang, X. Xu, M. Vacher and D. G. Truhlar, Nonadiabatic Coupling in Trajectory Surface Hopping: Accurate Time Derivative Couplings by the Curvature-Driven Approximation, *J. Chem. Theory Comput.*, 2023, **19**, 6577–6588.

37 J. Suchan, J. Janoš and P. Slavíček, Pragmatic Approach to Photodynamics: Mixed Landau–Zener Surface Hopping with Intersystem Crossing, *J. Chem. Theory Comput.*, 2021, **17**, 3444–3457.

38 J. J. Eriksen and J. Gauss, The Shape of Full Configuration Interaction to Come, *J. Phys. Chem. Lett.*, 2021, **12**, 418–427, for FCI exponential scaling.

39 A. J. Cohen, P. Mori-Sánchez and W. Yang, Challenges for Density Functional Theory, *Chem. Rev.*, 2012, **112**, 289–320, for DFT limitations in strong correlation.

40 L. Lacombe and N. T. Maitra, Non-adiabatic approximations in time-dependent density functional theory: progress and prospects, *npj Comput. Mater.*, 2023, **9**, 111, for DFT limitations in nonadiabatic regimes.

41 S. McArdle, S. Endo, A. Aspuru-Guzik, S. C. Benjamin and X. Yuan, Quantum computational chemistry, *Rev. Mod. Phys.*, 2020, **92**, 015003, for quantum computing in the electronic structure.

42 K. Head-Marsden, J. Flick, C. J. Ciccarino and P. Narang, Quantum Information and Algorithms for Correlated Quantum Matter, *Chem. Rev.*, 2021, **121**, 3061–3120, for quantum algorithms for correlated systems.

43 S. Lee, *et al.*, Evaluating the evidence for exponential quantum advantage in ground-state quantum chemistry, *Nat. Commun.*, 2023, **14**, 1952, for exponential speedup in quantum chemistry.

44 A. Aspuru-Guzik, A. D. Dutoi, P. J. Love and M. Head-Gordon, Simulated Quantum Computation of Molecular Energies, *Science*, 2005, **309**, 1704–1707.

45 M. Reiher, N. Wiebe, K. M. Svore, D. Wecker and M. Troyer, Elucidating Reaction Mechanisms on Quantum Computers, *Proc. Natl. Acad. Sci. U. S. A.*, 2017, **114**, 7555–7560.

46 A. Peruzzo, J. McClean, P. Shadbolt, M.-H. Yung, X.-Q. Zhou, P. J. Love, A. Aspuru-Guzik and J. L. O'brien, A variational eigenvalue solver on a photonic quantum processor, *Nat. Commun.*, 2014, **5**, 4213.

47 J. R. McClean, J. Romero, R. Babbush and A. Aspuru-Guzik, The theory of variational hybrid quantum-classical algorithms, *New J. Phys.*, 2016, **18**, 023023.

48 S. Zhao, D. Tang, X. Xiao, R. Wang, Q. Sun, Z. Chen, X. Cai, Z. Li, H. Yu and W.-H. Fang, Quantum Computation of Conical Intersections on a Programmable Superconducting Quantum Processor, *J. Phys. Chem. Lett.*, 2024, **15**, 7244–7253.

49 J. Preskill, Quantum Computing in the NISQ era and beyond, *Quantum*, 2018, **2**, 79.

50 O. Higgott, D. Wang and S. Brierley, Variational Quantum Computation of Excited States, *Quantum*, 2019, **3**, 156.

51 S. Belaloui, N. E. Belaloui and A. Benslama, On the Simulation of Conical Intersections in Water and Methanimine Molecules Via Variational Quantum Algorithms, *arXiv*, 2025, preprint, arXiv:2507.22670, DOI: [10.48550/arXiv.2507.22670](https://doi.org/10.48550/arXiv.2507.22670).

52 K. M. Nakanishi, K. Mitarai and K. Fujii, Subspace-search variational quantum eigensolver for excited states, *Phys. Rev. Res.*, 2019, **1**, 033062.

53 J. Robledo-Moreno, *et al.*, Chemistry beyond the scale of exact diagonalization on a quantum-centric supercomputer, *Sci. Adv.*, 2025, **11**(25), eadu9991.

54 S. Barison, J. Robledo Moreno and M. Motta, Quantum-centric computation of molecular excited states with extended sample-based quantum diagonalization, *Quantum Sci. Technol.*, 2025, **10**, 025034.

55 J. R. McClean, M. E. Kimchi-Schwartz, J. Carter and W. A. de Jong, Hybrid quantum-classical hierarchy for mitigation of decoherence and determination of excited states, *Phys. Rev. A*, 2017, **95**, 042308.

56 Y. Tong, V. V. Albert, J. Preskill and Y. Su, Generalized Quantum Subspace Expansion, *Phys. Rev. Lett.*, 2022, **129**, 020502.

57 T. Takeshita, N. C. Rubin, Z. Jiang, E. Lee, R. Babbush and J. R. McClean, Increasing the Representation Accuracy of Quantum Simulations of Chemistry without Extra Quantum Resources, *Phys. Rev. X*, 2020, **10**, 011004.

58 M. Urbanek, D. Camps, R. Van Beeumen and W. A. de Jong, Chemistry on Quantum Computers with Virtual Quantum Subspace Expansion, *J. Chem. Theory Comput.*, 2020, **16**, 5425–5431.

59 D. Alfonso, Y.-L. Lee, H. P. Paudel and Y. Duan, Chemical applications of variational quantum eigenvalue-based quantum algorithms: Perspective and survey, *Appl. Phys. Rev.*, 2025, **12**, 031304.

60 P. J. Ollitrault, A. Kandala, C.-F. Chen, M. Pistoia, A. Mezzacapo, K. Temme, M. Takita, J. Rice and A. J.-A. Martin, others Quantum equation of motion for computing molecular excitation energies on a noisy quantum processor, *Phys. Rev. Res.*, 2020, **2**, 043140.

61 H. R. Grimsley, N. I. Mayhall, D. Claudino, N. M. Tubman, C. A. Morrison, M. Metcalf, S. E. Economou and E. Barnes, Challenging excited states from adaptive quantum eigensolvers: subspace expansions vs. state-averaged strategies, *Quantum Sci. Technol.*, 2025, **10**, 025003.

62 A. Gandon, A. Baiardi, P. Ollitrault and I. Tavernelli, Nonadiabatic Molecular Dynamics with Fermionic Subspace-Expansion Algorithms on Quantum Computers, *J. Chem. Theory Comput.*, 2024, **20**, 5951–5963.

63 E. Sangiogo Gil, M. Oppel, J. S. Kottmann and L. González, SHARC meets TEQUILA: mixed quantum-classical dynamics on a quantum computer using a hybrid quantum-classical algorithm, *Chem. Sci.*, 2025, **16**, 596–609.

64 C. Hempel, C. Maier, J. Romero, J. McClean, T. Monz, H. Shen, P. Jurcevic, B. P. Lanyon, P. Love, R. Babbush, A. Aspuru-Guzik, R. Blatt and C. F. Roos, Quantum Chemistry Calculations on a Trapped-Ion Quantum Simulator, *Phys. Rev. X*, 2018, **8**, 031022.

65 A. Szabo and N. S. Ostlund, *Modern Quantum Chemistry: Introduction to Advanced Electronic Structure Theory*, Dover Publications, New York, 1989, Originally published by McGraw-Hill in 1982.

66 J. Tilly, P. Sriluckshmy, A. Patel, E. Fontana, I. Rungger, E. Grant, R. Anderson, J. Tennyson and G. H. Booth, Reduced density matrix sampling: Self-consistent embedding and multiscale electronic structure on current generation quantum computers, *Phys. Rev. Res.*, 2021, **3**, 033230.

67 D. S. King and L. Gagliardi, A Ranked-Orbital Approach to Select Active Spaces for High-Throughput Multireference Computation, *J. Chem. Theory Comput.*, 2021, **17**, 2817–2831.

68 Z. Luo, Y. Ma, C. Liu and H. Ma, Efficient Reconstruction of CAS-CI-Type Wave Functions for a DMRG State Using Quantum Information Theory and a Genetic Algorithm, *J. Chem. Theory Comput.*, 2017, **13**, 4699–4710.

69 W. Jeong, S. J. Stoneburner, D. King, R. Li, A. Walker, R. Lindh and L. Gagliardi, Automation of Active Space Selection for Multireference Methods via Machine Learning on Chemical Bond Dissociation, *J. Chem. Theory Comput.*, 2020, **16**, 2389–2399.

70 P. Jordan and E. Wigner, Über das Paulische Äquivalenzverbot, *Z. Phys.*, 1928, **47**, 631–651.

71 A. Peruzzo, J. McClean, P. Shadbolt, M.-H. Yung, X.-Q. Zhou, P. J. Love, A. Aspuru-Guzik and J. L. O'Brien, A variational eigenvalue solver on a photonic quantum processor, *Nat. Commun.*, 2014, **5**, 4213.

72 J. Tilly, others The Variational Quantum Eigensolver: A review of methods and best practices, *Phys. Rep.*, 2022, **986**, 1–45, reviews the CASCI-VQE method, detailing its application in quantum chemistry for computing adiabatic potential energy surfaces.

73 A. Asthana, A. Kumar, V. S. A. Abraham, P. A. Bhobe, A. K. Pal and T. S. Mahesh, Contextual subspace variational quantum eigensolver calculation of the dissociation curve of fermion-boson system on a superconducting quantum processor, *npj Quantum Inf.*, 2024, **10**, 25.

74 M. Matoušek, K. Pernal, F. Pavošević and L. Veis, Variational Quantum Eigensolver Boosted by Adiabatic Connection, *J. Phys. Chem. A*, 2024, **128**, 687–698.

75 W. Mizukami, K. Mitarai, Y. O. Nakagawa, Y. Ibe, Y. Koh and N. Koizumi, Orbital optimized unitary coupled cluster theory for quantum computer, *Phys. Rev. Res.*, 2020, **2**, 033421.

76 P. J. Ollitrault, A. Kandala, C.-F. Chen, M. Pistoia, A. Mezzacapo, K. Temme, M. Takita, J. Rice and A. J.-A. Martin, others Quantum equation of motion for computing molecular excitation energies on a noisy quantum processor, *Phys. Rev. Res.*, 2020, **2**, 043140.

77 A. Gandon, A. Baiardi, M. Rossmannek, W. Dobrautz and I. Tavernelli, Quantum computing in spin-adapted representations for efficient simulations of spin systems, *PRX Quantum*, 2025, **6**, 030306.

78 E. N. Epperly, L. Lin and Y. Nakatsukasa, A Theory of Quantum Subspace Diagonalization, *SIAM J. Matrix Anal. Appl.*, 2022, **43**, 1263–1290.

79 C. Umeano, F. M. C. Jamet, L. P. Lindoy, I. Rungger and O. Kyriienko, Quantum subspace expansion approach for simulating dynamical response functions of Kitaev spin liquids, *Phys. Rev. Mater.*, 2025, **9**, 034401.

80 N. Yoshioka, H. Hakoshima, Y. Matsuzaki, Y. Tokunaga, Y. Suzuki and S. Endo, Generalized Quantum Subspace Expansion, *Phys. Rev. Lett.*, 2022, **129**, 020502.

81 Z. Cai, Quantum Error Mitigation using Symmetry Expansion, *Quantum*, 2021, **5**, 548.

82 J. R. McClean, Z. Jiang, N. C. Rubin, R. Babbush and H. Neven, Decoding quantum errors with subspace expansions, *Nat. Commun.*, 2020, **11**, 636.

83 I. O. Sokolov, P. K. Barkoutsos, L. Moeller, P. Suchsland, G. Mazzola and I. Tavernelli, Microcanonical and finite-temperature ab initio molecular dynamics simulations on quantum computers, *Phys. Rev. Res.*, 2021, **3**, 013125.

84 T. E. O'Brien, M. Streif, N. C. Rubin, R. Santagati, Y. Su, W. J. Huggins, J. J. Goings, N. Moll, E. Kyoseva, M. Degroote, C. S. Tautermann, J. Lee, D. W. Berry, N. Wiebe and R. Babbush, Efficient quantum computation of molecular forces and other energy gradients, *Phys. Rev. Res.*, 2022, **4**, 043210.

85 P. Pulay, Analytical derivatives, forces, force constants, molecular geometries, and related response properties in electronic structure theory, *Wiley Interdiscip. Rev.: Comput. Mol. Sci.*, 2014, **4**, 169–181, for finite differences and Pulay forces in MO-based methods.

86 I. N. Levine, *Quantum Chemistry*, Pearson, 6th edn, 2009, For the Hellmann–Feynman theorem derivation and its application to variational wavefunctions.

87 J. Lai, Y. Fan, Q. Fu, Z. Li and J. Yang, Accurate and efficient calculations of Hellmann–Feynman forces for quantum

computation, *J. Chem. Phys.*, 2023, **159**, 114113, for the Hellmann–Feynman theorem in the context of VQE and analytical gradients.

88 S. Pathak, I. E. López, A. J. Lee, W. P. Bricker, R. L. Fernández, S. Lehtola and J. A. Rackers, Accurate Hellmann–Feynman forces from density functional calculations with augmented Gaussian basis sets, *J. Chem. Phys.*, 2023, **158**, 014104, for Pulay forces and basis set dependence in Hellmann-Feynman calculations.

89 T. E. O'Brien, B. Senjean, R. Sagastizabal, X. Bonet-Monroig, A. Dutkiewicz, F. Buda, L. DiCarlo and L. Visscher, Calculating energy derivatives for quantum chemistry on a quantum computer, *npj Quantum Inf.*, 2019, **5**, 113, for derivative Hamiltonian and force operators in VQE, including MO-based force calculations.

90 J. Jiří, S. Petr and B. F. E. Curchod, Selecting Initial Conditions for Trajectory-Based Nonadiabatic Simulations, *Acc. Chem. Res.*, 2025, **58**(2), DOI: 10.1021/acs.accounts.4c00687.

91 M. Barbatti, S. Mai, M. Richter, M. Ruckenbauer, B. P. Fingerhut, F. Plasser, T. Schnappinger, M. Oppel, P. Marquetand, K. Sen and H. Lischka, Newton-X Platform: New Software Developments for Surface Hopping and Nuclear Ensembles, *J. Chem. Theory Comput.*, 2022, **18**, 6851–6865.

92 J. Suchan, D. Hollas, B. F. E. Curchod and P. Slav'iček, On the importance of initial conditions for excited-state dynamics, *Faraday Discuss.*, 2018, **212**, 307–330.

93 D. A. McQuarrie and J. D. Simon, *Physical Chemistry: A Molecular Approach*, 2000, Provides a detailed explanation of Wigner sampling and the Wigner distribution for harmonic oscillators in phase space, suitable for initializing quantum nuclear effects.

94 C. F. Kammerer and P. Gérard, *Wigner Measures and Molecular Propagation Through Generic Energy Level Crossings*, Prépublication de l'Université de Cergy-Pontoise, 2002, Discusses Wigner measures in the context of molecular propagation, relevant for understanding Wigner sampling in nonadiabatic dynamics.

95 X. Bian, *et al.*, Quantum Solver of Contracted Eigenvalue Equations (QSE) for Quantum Chemistry, *J. Chem. Theory Comput.*, 2021, **17**, 2854–2866, describes the quantum solver of contracted eigenvalue equations (QSE) for computing potential energy surfaces in quantum chemistry.

96 M. Barbatti, Nonadiabatic dynamics with trajectory surface hopping in the adiabatic representation, *J. Chem. Phys.*, 2011, **135**, 174102, details the detection of local minima in energy gaps for surface hopping and handling of nonadiabatic transitions without explicit coupling vectors.

97 G. A. Hagedorn, Proof of the Landau–Zener formula in an adiabatic limit with small eigenvalue gaps, *Commun. Math. Phys.*, 1991, **136**, 433–449, provides a rigorous mathematical analysis of the Landau–Zener formula, foundational for nonadiabatic transition probabilities in LZSH.

98 L. Wang, *et al.*, A class of Landau-Zener type surface hopping algorithms, *J. Chem. Phys.*, 2014, **140**, 124106, compares Landau–Zener formulae for nonadiabatic transition probabilities, including their application in surface hopping algorithms.

99 N. Sisourat, *et al.*, Ultrafast dynamics of H2O+ following photoionization in the 20-35 eV energy range, *J. Chem. Phys.*, 2015, **142**, 104307, describes a practical implementation of Landau–Zener surface hopping for water molecule photodynamics, including input file specifications and velocity rescaling.

100 T. Jíra, J. Janoš and P. Slavíček, Critical Assessment of Curvature-Driven Surface Hopping Algorithms, *J. Chem. Theory Comput.*, 2025, **21**, 9784–9798.

101 W. Mizukami, Chemqulacs: Quantum chemistry code for quantum circuit simulators and quantum computers, GitHub repository, 2025, https://github.com/wmizukami/chemqulacs, accessed on August 16, 2025.

102 M. Barbatti, *et al.*, Newton-X Platform: New Software Developments for Surface Hopping and Nuclear Ensembles, *J. Chem. Theory Comput.*, 2022, **18**, 6851–6865.

103 X. Xu, *et al.*, MindSpore Quantum: A User-Friendly, High-Performance, and AI-Compatible Quantum Computing Framework, *arXiv*, 2024, preprint, arXiv:2406.17248, DOI: 10.48550/arXiv.2406.17248.

104 Inc., Q, Contributors QURI Parts: An open source library suite for creating and executing quantum algorithms on various quantum computers and simulators, https://github.com/QunaSys/quri-parts, 2022.

105 Y. Suzuki, *et al.*, Qulacs: a fast and versatile quantum circuit simulator for research purpose, *Quantum*, 2021, **5**, 559.

106 P. O. Dral, MLatom: A Program Package for Quantum Chemical Research Assisted by Machine Learning, *J. Comput. Chem.*, 2019, **40**, 2339–2347.

107 P. O. Dral, F. Ge, B.-X. Xue, Y.-F. Hou, M. Pinheiro Jr, J. Huang and M. Barbatti, MLatom 2: An Integrative Platform for Atomistic Machine Learning, *Top. Curr. Chem.*, 2021, **379**, 27.

108 P. O. Dral, *et al.*, MLatom 3: A Platform for Machine Learning-Enhanced Computational Chemistry Simulations and Workflows, *J. Chem. Theory Comput.*, 2024, **20**, 1193–1213.

109 P. O. Dral, *et al.*, *MLatom: A Package for Atomistic Simulations with Machine Learning*, 2013–2024.

110 Q. Sun, *et al.*, Recent developments in the PySCF program package, *J. Chem. Phys.*, 2020, **153**, 024109.

111 A. Anand, P. Schleich, S. Alperin-Lea, P. W. K. Jensen, S. Sim, M. Díaz-Tinoco, J. S. Kottmann, M. Degroote, A. F. Izmaylov and A. Aspuru-Guzik, A quantum computing view on unitary coupled cluster theory, *Chem. Soc. Rev.*, 2022, **51**, 1659–1684.

112 J. Lee, W. J. Huggins, M. Head-Gordon and K. B. Whaley, Generalized Unitary Coupled Cluster Wave functions for Quantum Computation, *J. Chem. Theory Comput.*, 2018, **15**, 311–324.

113 D. C. Liu and J. Nocedal, On the limited memory BFGS method for large scale optimization, *Math. Program.*, 1989, **45**, 503–528.

114 X.-H. Zha, C. Zhang, D. Fan, P. Xu, S. Du, R.-Q. Zhang and C. Fu, The impacts of optimization algorithm and basis size on the accuracy and efficiency of variational quantum eigensolver, *arXiv*, 2021, preprint, arXiv:2006.15852, DOI: 10.48550/arXiv.2006.15852.

115 S. Mukherjee, D. Mukhopadhyay and S. Adhikari, Conical intersections and diabatic potential energy surfaces for the three lowest electronic singlet states of H_3^+, *J. Chem. Phys.*, 2014, **141**, 204306.

116 S. Saade and H. G. A. Burton, Excited State-Specific CASSCF Theory for the Torsion of Ethylene, *J. Chem. Theory Comput.*, 2024, **20**, 3466–3477.

117 H.-J. Werner, P. J. Knowles, G. Knizia, F. R. Manby and M. Schütz, Molpro: a general-purpose quantum chemistry program package, *WIREs Comput. Mol. Sci.*, 2012, **2**, 242–253.

118 D. G. A. Smith, *et al.*, PSI4 1.4: Open-source software for high-throughput quantum chemistry, *J. Chem. Phys.*, 2020, **152**, 184108.